Published in final edited form as:

Neuron. 2017 September 27; 96(1): 190–206.e7. doi:10.1016/j.neuron.2017.09.014.

Aldosterone-Sensing Neurons in the NTS Exhibit State-Dependent Pacemaker Activity and Drive Sodium Appetite via Synergy with Angiotensin II Signaling

Jon M. Resch[1,7], **Henning Fenselau**[1,7], **Joseph C. Madara**[1,7], **Chen Wu**[1], **John N. Campbell**[1], **Anna Lyubetskaya**[1], **Brian A. Dawes**[1], **Linus T. Tsai**[1], **Monica M. Li**[1], **Yoav Livneh**[1], **Qingen Ke**[2], **Peter M. Kang**[2], **Géza Fejes-Tóth**[3], **Anikó Náray-Fejes-Tóth**[3], **Joel C. Geerling**[4,6,8], and **Bradford B. Lowell**[1,5,8,*]

[1]Division of Endocrinology, Diabetes, and Metabolism, Department of Medicine, Beth Israel Deaconess Medical Center, Harvard Medical School, Boston, Massachusetts, 02215, USA

[2]Cardiovascular Division, Beth Israel Deaconess Medical Center, Harvard Medical School, Boston, Massachusetts, 02215, USA

[3]Department of Physiology and Neurobiology, Geisel School of Medicine at Dartmouth, Lebanon, New Hampshire, 03755 USA

[4]Department of Neurology, Beth Israel Deaconess Medical Center, Harvard Medical School, Boston, Massachusetts, 02215, USA

[5]Program in Neuroscience, Harvard Medical School, Boston, Massachusetts, 02115, USA

Summary

Sodium deficiency increases angiotensin II (ATII) and aldosterone, synergistically stimulating its retention and consumption. Recently, ATII-responsive neurons in the subfornical organ (SFO) and aldosterone-sensitive neurons in the nucleus of the solitary tract (NTS^{HSD2} neurons) were shown to drive sodium appetite. Here we investigate the basis for NTS^{HSD2} neuron activation, identify the circuit by which NTS^{HSD2} neurons drive appetite, and uncover an interaction between the NTS^{HSD2} circuit and ATII signaling. NTS^{HSD2} neurons respond to sodium deficiency with

Correspondence: Joel C. Geerling, MD, PhD, joel-geerling@uiowa.edu, Department of Neurology, Carver College of Medicine, University of Iowa, 200 Hawkins Drive, Iowa City, IA 52242, Bradford B. Lowell, MD, PhD, blowell@bidmc.harvard.edu, Division of Endocrinology, Diabetes, and Metabolism, Department of Medicine, Beth Israel Deaconess Medical Center, Center for Life Sciences, Rm-703, 3 Blackfan Circle, Boston, MA 02115.

[6]Current Address: Department of Neurology, University of Iowa Carver College of Medicine, Iowa City, Iowa, 52242, USA

[7]These authors contributed equally

[8]Co-corresponding authors

[*]Lead Contact

AUTHOR CONTRIBUTIONS

Conceptualization, J.M.R, H.F., J.C.G., and B.B.L.; Methodology, J.M.R, H.F., J.C.M., J.N.C., A.L., M.M.L., J.C.G., and B.B.L.; Validation, J.M.R, H.F., J.C.M., and C.W.; Formal Analysis; J.M.R., H.F., J.C.M., J.N.C., A.L., and B.A.D.; Investigation, J.M.R, H.F., J.C.M., C.W., J.N.C., Q.K., and J.C.G.; Resources, P.M.K., G.F.-T., A.N.-F.-T., and B.B.L.; Writing – Original Draft, J.M.R., J.C.G., and B.B.L.; Writing – Review & Editing, J.M.R, H.F., J.C.M., J.N.C., Y.L. J.C.G., and B.B.L.; Funding Acquisition, J.M.R. and B.B.L.

spontaneous pacemaker-like activity – the consequence of "cardiac" HCN and $Na_v1.5$ channels. Remarkably, NTS^{HSD2} neurons are necessary for sodium appetite, and with concurrent ATII signaling their activity is sufficient to produce rapid consumption. Importantly, NTS^{HSD2} neurons stimulate appetite via projections to the vlBNST, which is also the effector site for ATII-responsive SFO neurons. The interaction between angiotensin signaling and NTS^{HSD2} neurons provides a neuronal context for the long-standing "synergy hypothesis" of sodium appetite regulation.

INTRODUCTION

Sodium (Na^+) and its salts are the major osmotically active solutes of the extracellular fluid. Consequently, when Na^+ is deficient, extracellular volume contracts and the effective circulatory volume falls (hypovolemia). The latter leads to increased levels of angiotensin II (ATII) which then stimulates secretion of the primary mineralocorticoid, aldosterone (Eaton and Pooler, 2013). Together, these hormones target the kidney to reduce Na^+ excretion (Eaton and Pooler, 2013), and the brain to increase sodium appetite (Epstein, 1992). Both responses involve synergistic actions of ATII and aldosterone.

The synergy between ATII and aldosterone is important because, in addition to regulating Na^+ excretion, aldosterone also regulates potassium (K^+) (Eaton and Pooler, 2013). Increases in blood K^+ (hyperkalemia) strongly stimulate aldosterone secretion, which then promotes renal excretion of K^+ – a vital process given dietary intake of K^+ and the importance of preventing hyperkalemia. This capacity for aldosterone to preferentially promote Na^+ retention during Na^+ deficiency and K^+ excretion during hyperkalemia has been termed “the aldosterone paradox” (Arroyo et al., 2011). The paradox is resolved by ATII. In the case of Na^+ deficiency and hypovolemia, elevated ATII and aldosterone synergistically increase Na^+ reabsorption, and in addition, ATII reduces the extent of aldosterone-stimulated K^+ excretion. Hyperkalemia, however, stimulates only aldosterone. In this state, aldosterone drives K^+ excretion, and Na^+ reabsorption is enhanced, but less so than in hypovolemia due to the lack of ATII. Thus, aldosterone action is biased towards increasing Na^+ reabsorption when ATII is high, and K^+ excretion when ATII is low.

Given the dual roles for aldosterone in the kidney, the brain may have also developed a mechanism to maximally drive sodium appetite when deficient, but less so when aldosterone is increased during hyperkalemia. With this in mind, it is of interest that sodium appetite involves synergy between ATII and aldosterone (Epstein, 1992). ATII and aldosterone signaling are both critical for deficiency-induced appetite (Matsuda et al., 2017; Sakai et al., 1986), and, in non-depleted animals, sodium appetite is synergistically induced by simultaneous administration of ATII and mineralocorticoids (Fluharty and Epstein, 1983). This synergy between ATII and aldosterone in appetite likely allows for smaller deficiencies of Na^+ to stimulate appetite – hence, preemptively warding off larger disturbances and their adverse circulatory consequences (Sakai et al., 1986). Furthermore, it may also protect against exaggerated Na^+ ingestion when aldosterone is elevated but Na^+ deficiency does not exist (e.g., hyperkalemia).

The neural substrate responsible for ATII- and aldosterone-mediated sodium appetite is increasingly being understood. In regards to the former, neurons in the subfornical organ

(SFO) expressing the ATII type 1a receptor (AT1aR) play an important role. Supporting this, SFO-specific knockout of AT1aRs suppresses Na^+ intake induced by Na^+ deficiency. Likewise, inhibition of VGLUT2-expressing SFO neurons that project to the ventral bed nucleus of the stria terminalis (vBNST) eliminates sodium appetite (Matsuda et al., 2017). These data strongly suggest the existence of glutamatergic ATII-sensitive SFO neurons that regulate sodium appetite via projections to the vBNST.

For aldosterone-mediated sodium appetite, focus has been on neurons in the nucleus of the solitary tract (NTS) marked by expression of 11β-hydroxysteroid dehydrogenase 2 (HSD2; NTS^{HSD2} neurons). HSD2 expression is a necessary precondition for aldosterone-sensing cells. It is required to inactivate glucocorticoids, which, because of their high affinity for the mineralocorticoid receptor (MR) and abundance, would otherwise cause indiscriminate activation of MRs (Naray-Fejes-Toth et al., 1998). Consistent with expression of HSD2 and MR, NTS^{HSD2} neurons exhibit Fos immunoreactivity after administration of MR agonists (Geerling et al., 2006). Furthermore, NTS^{HSD2} neuron Fos activation during Na^+ deficiency closely tracks the onset and offset of sodium appetite (Geerling et al., 2006; Geerling and Loewy, 2006b). The cellular mechanism by which NTS^{HSD2} neurons become active during Na^+ deficiency is presently unknown. Given that NTS^{HSD2} neurons express HSD2 and MR, it likely involves aldosterone and cell-autonomous effects on gene expression. Whether NTS^{HSD2} neurons are also activated by ATII and/or receive vagal afferent feedback that signals the effective circulatory volume is unclear. Importantly, consistent with their hypothesized role in driving sodium appetite, it was recently shown using chemogenetics that NTS^{HSD2} neurons are necessary and sufficient for full development of sodium appetite (but more later on their sufficiency) (Jarvie and Palmiter, 2017).

In the present study, we use brain slice electrophysiology and single neuron RNA sequencing (RNA-Seq) to determine the cellular and molecular mechanism by which NTS^{HSD2} neurons are activated by Na^+ deficiency. We then use genetic ablation and chemogenetic activation to study their role in driving sodium appetite. Because NTS^{HSD2} neurons appear to be the neuronal embodiment of the “aldosterone signal”, we also pursue the hypothesis that, like the kidney, maximal induction of sodium appetite occurs through synergy between NTS^{HSD2} neurons and ATII signaling. Finally, we use anterograde tracing, Channelrhodopsin (ChR2)-assisted circuit mapping, and optogenetic terminal stimulation to establish the downstream site by which NTS^{HSD2} neurons cause sodium appetite.

RESULTS

Sodium Deficiency Increases the Firing of NTS^{HSD2} Neurons

To visualize NTS^{HSD2} neurons for electrophysiology, *Hsd11b2-Cre* knockin mice (Naray-Fejes-Toth and Fejes-Toth, 2007) were crossed with Ai9tdTomato reporter mice. HSD2 immunofluorescence revealed that >85% of HSD2-positive neurons expressed tdTomato, and that very few tdTomato-expressing cells lacked HSD2 in the NTS (~5% of all $tdTomato^+$ cells) (Figure S1A). Thus, tdTomato expression in *Hsd11b2-Cre*::Ai9tdTomato mice marks the majority of NTS^{HSD2} neurons.

Two standard approaches were used to create Na^+ deficiency, either furosemide-induced Na^+ diuresis followed by one day of low-sodium diet or chronic low-sodium diet for 8–12 days (Figure S1B). Control mice for both protocols were treated identically as the Na^+ deficient group but were fed standard chow. Both approaches increased blood aldosterone levels by ~ 2-fold (Table S1).

We first performed recordings in whole-cell mode to assay NTS^{HSD2} neuron activity in response to Na^+ deprivation. NTS^{HSD2} neurons in *ex vivo* brain slices were synaptically isolated by adding blockers of AMPA, kainate, NMDA and GABA-A receptors. Chronic low-sodium diet markedly increased the action potential (AP) firing of NTS^{HSD2} neurons (Figure S1C,D). However, these recordings in whole-cell mode were complicated by an unusually large and rapid "rundown" in membrane potential and firing rate (Figure S1E), making it difficult to establish a stable baseline. This rundown could be due to hyperpolarization-activated cyclic nucleotide-gated (HCN) channels (Pian et al., 2006), which we later discover are highly expressed and very active in NTS^{HSD2} neurons (see Figure 2D & Figure 3).

To avoid rundown, we recorded AP firing rates in loose-seal cell-attached configuration (Figure 1A). Again, studies were performed in the presence of synaptic blockers. NTS^{HSD2} neurons from control mice showed very low rates of firing – the majority at less than 0.5 hertz (Hz; Figure 1B,C). By contrast, in Na^+-deficient mice, NTS^{HSD2} neurons fired at rates averaging ~ 2 Hz after furosemide diuresis (Figure 1B) and ~ 3 Hz after chronic low-sodium diet (Figure 1C). The neighboring HSD2-negative NTS neurons were either silent or firing at very low rates, and this was true for neurons from both control and Na^+-deficient mice (Figure 1D). Thus, Na^+ deficiency selectively increases the firing of NTS^{HSD2} neurons.

To evaluate if aldosterone has rapid, possibly non-genomic, actions on NTS^{HSD2} neurons, we recorded their activity during bath application of aldosterone for 30 minutes in *ex vivo* brain slices. This had no effect on the firing rate of NTS^{HSD2} neurons (Figure 1E). Failing to see rapid effects, we then undertook an *in vivo* chronic administration approach using osmotic minipumps filled with vehicle or aldosterone (Figure S1B). Electrophysiological brain slice studies were performed 8–12 days post implantation. By this time, aldosterone had increased to a level comparable to that seen in Na^+-deficient mice (Table S1) and increased the firing rate of NTS^{HSD2} neurons (Figure 1F). However, the observed increase in many neurons was not as high as that seen with Na^+ deprivation. This raises the possibility that some factor, in addition to aldosterone, further increases NTS^{HSD2} neuron activity in the Na^+-deficient state. This factor might be ATII as in later RNA-Seq studies (see Figure 2B) we discover that NTS^{HSD2} neurons express abundant AT1aR mRNA. Consistent with this, bath application of ATII markedly increased the firing rate of NTS^{HSD2} neurons, and the AT1aR-selective blocker, losartan, blocked this effect (Figure 1G,H). We then tested the ability of ATII to augment the AP firing of NTS^{HSD2} neurons from mice treated with chronic aldosterone minipumps. Indeed, bath application of ATII further increased the firing rate of NTS^{HSD2} neurons under these conditions (Figure 1I) suggesting the combination of aldosterone and ATII signaling may maximally drive NTS^{HSD2} neuron activity during Na^+ deficiency.

Finally, we investigated whether NTS^{HSD2} neurons receive vagal afferent input, which might relay information about the effective circulatory volume, using ChR2-assisted circuit mapping (CRACM). To accomplish this, nodose ganglia of *Hsd11b2-Cre*::Ai9tdTomato mice were injected with AAV expressing ChR2 (Chang et al., 2015) (Figure S2A,B), and we recorded light-evoked postsynaptic currents from NTS neurons within the vagal afferent terminal field in *ex vivo* brain slices. For HSD2-negative NTS neurons, we readily detected glutamatergic inputs (11 out of 20) from vagal afferents, many of which were likely monosynaptic given their short response latency (Figure S2C,D). For NTS^{HSD2} neurons, however, we detected vagal inputs to only 3 out of 59 neurons tested across four mice, and these were likely all polysynaptic as they had long latencies (> 15 ms) (Figure S2C,D). We further tested 1 of the 3 responding NTS^{HSD2} neurons for monosynaptic connectivity with vagal afferents by adding tetrodotoxin (TTX) and 4-aminopyridine (4-AP) to the bath. Under these conditions, light-evoked currents are completely dependent on ChR2 as local network activity is inhibited by TTX. This treatment abolished the light-evoked current further supporting a lack of monosynaptic input. Lack of vagal input to NTS^{HSD2} neurons is consistent with the previous finding that most NTS^{HSD2} neurons receive few or no close contacts from boutons labeled by biotinylated dextran amine injected into the nodose ganglia (Shin et al., 2009). Thus, NTS^{HSD2} neurons are regulated by ATII and aldosterone, and may not be directly regulated by vagal afferent input. Given that our studies were performed on synaptically isolated neurons, these results indicate that Na^+ deficiency may augment the activity of NTS^{HSD2} neurons in a cell-autonomous manner.

Single Cell RNA Sequencing of NTS^{HSD2} Neurons

Given that Na^+ deficiency increases the activity of synaptically isolated NTS^{HSD2} neurons, and this is likely driven, at least in part, by aldosterone/MR-regulated transcription, we hypothesized that changes in expression of ion channels or their regulatory proteins produce the state-dependent, pacemaker-like activity. Genes of interest could constitutively confer the latent capacity for pacemaker activity (Khaliq and Bean, 2010), or, by increased expression, stimulate neuronal activity in the Na^+-deficient state. As will be demonstrated below, our efforts uncovered examples of both.

We assessed gene expression by performing single neuron RNA-Seq. Specifically, *Hsd11b2-Cre*::Ai9tdTomato mice were fed either standard chow or low-sodium diet for 8–12 days, and NTS^{HSD2} neurons were then manually picked for subsequent RNA profiling (Figure 2A). Characterization of neurons from control (n = 33) and Na^+-deficient (n = 32) conditions that passed quality control is shown in Figure 2B. Each expressed beta-actin (*Actb*), the neuronal markers *Tubb3* and *Syn1*, little or no glial cell markers (*Gfap, Aif1*, and *Olig1*), the region-specific NTS marker *Phox2b*, and, as expected, HSD2 (*Hsd11b2*) and MR (*Nr3c2*). They also expressed VGLUT2 (*Slc17a6*), but little or no VGAT (*Slc32a1*) or *Th*. Thus, NTS^{HSD2} neurons were successfully sequenced, and they are glutamatergic. Consistent with the latter, we found that HSD2 protein co-localized with Cre-dependent GFP reporter in the NTS of VGLUT2-IRES-Cre mice, but not in VGLUT3-IRES-Cre or VGAT-IRES-Cre mice (Figure S3). Finally, in agreement with electrophysiology experiments showing that ATII increased their firing rate (Figure 1G), NTS^{HSD2} neurons expressed AT1aR transcript

(*Agtr1a*) (Figure 2B). Indeed, *Agtr1a* was the 5th most abundant GPCR, expressed by 97% of NTS^{HSD2} neurons.

Comparing NTS^{HSD2} neurons between control and Na^+-deficient mice revealed a large number of genes that were significantly upregulated (606) or downregulated (17) by Na^+ deficiency (Table S2). First, we considered canonical targets of aldosterone/MR signaling, but this analysis was of limited value because knowledge of genes selectively targeted by aldosterone/MR is incomplete – especially for the brain (Viengchareun et al., 2007). Known target genes of theoretical interest, including the aldosterone-inducible subunits of the renal epithelial Na^+ channel, ENaC (*Scnn1a, Scnn1b and Scnn1g*), which also serves as the taste receptor for salt, were absent in control and deprived NTS^{HSD2} neurons (Figure S4A). Furthermore, consistent with the lack of a role for this otherwise attractive candidate (Fu and Vallon, 2014), the ENaC blocker amiloride did not inhibit firing of NTS^{HSD2} neurons from Na^+-deprived mice (Figure S4C). On the other hand, NTS^{HSD2} neurons did express the aldosterone/MR target gene, serum/glucocorticoid regulated kinase 1 (*Sgk1*), which in the kidney mediates aldosterone-induced trafficking of ion channels. However, its expression was not upregulated in neurons from Na^+-deficient mice. Of the known aldosterone/MR target genes (Viengchareun et al., 2007) expressed in NTS^{HSD2} neurons (Figure S4A,B), two were significantly upregulated by Na^+ deficiency: WNK lysine deficient protein kinase 1 (*Wnk1*) and the α1 subunit of Na+/K+-ATPase pump (*Atp1a1*). The meaning of *Wnk1* upregulation is unclear, however, since NTS^{HSD2} neurons lack its ion flux-regulating phosphorylation targets (Hadchouel et al., 2016). The meaning of *Atp1a1* upregulation is similarly unclear, as it seems to be an unlikely mediator of increased NTS^{HSD2} neuron firing.

We next looked at mRNA expression of ion channels defined by the IUPHAR (Southan et al., 2016) (Figure 2C and Table S3) and more specifically, at channels known to support pacemaker-like activity (Khaliq and Bean, 2010) (Figure 2D–F). These include the nonselective cation “leak” channel, NALCN; the HCN channels which are activated by hyperpolarization and bring cells to a more depolarized resting membrane potential; various voltage-gated Ca^{2+} channels that have depolarizing subthreshold currents; and voltage-gated Na^+ channels that have “persistent” depolarizing Na^+ currents (I_{NaP}) at subthreshold voltages. *Nalcn* was abundantly expressed by NTS^{HSD2} neurons, but it was not induced by Na^+ deficiency (Figure 2D). Thus, it may provide a background leak current which enables pacemaking and/or its activity might be regulated (Ren, 2011) – hypothetically by ATII/AT1aR-mediated signaling. Of interest, mRNA from all four HCN channels was detected in NTS^{HSD2} neurons (Figure 2D). *Hcn3* was most abundant, and *Hcn2* was significantly induced by Na^+ deficiency. These findings could be important because HCN channels are essential for pacemaking in the cardiac sinoatrial node and some spontaneously active neurons (Wahl-Schott and Biel, 2009). With regards to voltage-gated calcium (Ca^{2+}) channels (Figure 2E), Na^+ deficiency significantly upregulated *Cacna1i* (Ca_v 3.3; T-type), *Cacna1e* (Ca_v2.3; R-type), *Cacna1c* (Ca_v1.2; L-type) and *Cacna1b* (Ca_v2.2; N-type). As expected, NTS^{HSD2} neurons express multiple voltage-gated Na^+ channels (Figure 2F), and Na^+-deprivation produced a 2-fold increase in *Scn2a1* (Na_v1.2). Surprisingly, we found that NTS^{HSD2} neurons express the “cardiac” Na^+-channel gene, *Scn5a* (Na_v1.5). Na_v1.5 is a TTX-resistant Na^+ channel with an undefined role in CNS neurons. It regulates cardiac

rhythmicity (Lei et al., 2007) and is important for spontaneous firing of olfactory sensory neurons (Frenz et al., 2014). Thus, a number of likely mediators of spontaneous pacemaker-like activity are present in NTS^{HSD2} neurons, and many increase their expression with Na^+ deficiency.

HCN Channels are Permissive for NTS^{HSD2} neuron Pacemaker Activity

We used *ex vivo* brain slices from control and Na^+-deprived *Hsd11b2-Cre*::Ai9tdTomato mice to assess activity of HCN channels in NTS^{HSD2} neurons. To accomplish this, a sequential hyperpolarizing voltage-step protocol was applied to elicit HCN I_h currents (Figure 3A,B) (Fu et al., 1997). Consistent with the gene expression studies, we detected large I_h currents in NTS^{HSD2} neurons. Neighboring NTS neurons, however, displayed little or no I_h current (Figure 3A,B). Thus, HCN channel activity is a special property of NTS^{HSD2} neurons. Of note, I_h current was of equal magnitude in NTS^{HSD2} neurons from control versus Na^+-deficient mice suggesting that Na^+ deficiency does not augment HCN channel activity (Figure 3B). Alternatively, it is possible that HCN channel activity is stimulated by Na^+ deficiency *in vivo*, but our *ex vivo* slice preparations are not capable of detecting this effect. This could occur if crucial endogenously produced GPCR ligands are absent in our *ex vivo* experiments, and/or if rundown during whole-cell voltage-clamp recordings (Figure S1E) masks increased HCN channel activity. Nevertheless, resting membrane potentials in both states were similarly, relatively depolarized (Figure 3C), further supporting unchanged I_h in NTS^{HSD2} neurons between Na^+ states. Importantly, blockade of HCN channels in NTS^{HSD2} neurons from Na^+-deprived mice, by either cesium or ZD7288, inhibited the spontaneous activity of NTS^{HSD2} neurons (Figure 3D,E). In total, these data indicate that HCN channels in NTS^{HSD2} neurons confer a latent capacity for pacemaker activity. But because their activity is not increased further by Na^+ deprivation, they presumably work in concert with other channels to produce state-dependent firing.

The Cardiac TTX-Resistant Channel, $Na_v1.5$, Promotes State-Dependent NTS^{HSD2} Neuron Firing

RNA-Seq identified many channels whose increased subthreshold currents could collaborate with HCN channels to bring about state-dependent firing. One example is *Cacna1i*, (Figure 2E), which encodes the low voltage-activated T-type Ca^{2+} channel $Ca_v3.3$. Its increased expression (Figure 2C and 2E) prompted us to examine T-type currents in NTS^{HSD2} neurons, which we evoked using a standard voltage step approach (Dreyfus et al., 2010). Remarkably, very large currents were evoked in NTS^{HSD2} neurons from Na^+-deficient mice, while only small currents were evoked in NTS^{HSD2} neurons from control mice (Figure 4A,B). Importantly, no currents were evoked from neighboring non-HSD2 NTS neurons (Figure 4C). Thus, this large evoked current is a unique feature of NTS^{HSD2} neurons, and it is markedly increased by the Na^+-deficient state. However, surprisingly, the T-type Ca^{2+} channel antagonist, TTA-A2, did not block this current (Figure S5A) – hence it is not mediated by T-type Ca^{2+} channels.

We next investigated the role of voltage-gated Na^+ channels in mediating this state-dependent evoked current. While 1 μM TTX was present in the above-mentioned recordings, it is noteworthy that NTS^{HSD2} neurons express the TTX-resistant, cardiac, voltage-gated

Na^+ channel, $Na_v1.5$ (*Scn5a*). Unlike most voltage-gated Na^+ channels, it has a higher IC_{50} for TTX (~2 μM) and thus requires higher concentrations of TTX for effective blockade (Goldin, 2001). To determine if $Na_v1.5$ mediates this current, we repeated our voltage step recordings in the presence of either 1 or 10 μM TTX (Figure 4D). In NTS^{HSD2} neurons from control mice, as before, we observed small evoked currents in the presence of 1 μM TTX, which were blocked by 10 μM TTX. In NTS^{HSD2} neurons from Na^+-deprived mice, again we observed large evoked currents in the presence of 1 μM TTX, which were eliminated by addition of 10 μM TTX. Thus, $Na_v1.5$ likely mediates this state-dependent evoked current in NTS^{HSD2} neurons. Note that NTS^{HSD2} neurons do not express the two other TTX-resistant channels, $Na_v1.8$ (*Scn10a*) and $Na_v1.9$ (*Scn11a*) (Figure 2F).

To further evaluate the role of $Na_v1.5$, we examined the ability of cadmium (Cd^{2+}) to inhibit the state-dependent evoked current. Cd^{2+}, which blocks TTX-resistant voltage-gated Na^+ channels and voltage-gated Ca^{2+} channels (Fox et al., 1987; Frelin et al., 1986), attenuated the state-dependent evoked current (Figure S5C), and significantly reduced firing of Na^+-deprived NTS^{HSD2} neurons (Figure S5D). To determine if Cd^{2+} could decrease firing independently of $Na_v1.5$, we tested whether Cd^{2+} inhibited activity in another neuron. We chose hunger-promoting agouti-related peptide (AgRP) neurons for this control experiment because they do not express $Na_v1.5$ (Henry et al., 2015). Cd^{2+} did not affect the firing of AgRP neurons (Figure S5E). These findings with Cd^{2+} are consistent with the view that $Na_v1.5$ contributes to state-dependent firing of NTS^{HSD2} neurons.

Of interest, $Na_v1.5$ is uniquely sensitive to extracellular application of the cell-impermeant lidocaine derivative QX-314 (Figure 4E) (Qu et al., 1995). With this in mind, we assessed the effects of extracellular QX-314. Indeed, QX-314 reduced evoked currents (Figure 4F), further suggesting that $Na_v1.5$ mediates this current. Furthermore, QX-314 modestly reduced spontaneous firing of Na^+-deprived NTS^{HSD2} neurons (Figure 4G), and as with Cd^{2+}, QX-314 did not reduce the firing of AgRP neurons (Figure 4H). While Cd^{2+} and QX-314 were equally effective in blocking the evoked current, Cd^{2+} was more effective than QX-314 in inhibiting firing. We hypothesized that this was due to Cd^{2+} blocking voltage-gated Ca^{2+} channels in addition to $Na_v1.5$. To test this, we co-applied a cocktail of voltage-gated Ca^{2+} channel blockers (CCB) and QX-314 (Figure S5G). Although application of the CCB cocktail, by itself, had no effect on firing (Figure S5F–G), co-application of CCB and QX-314 produced marked inhibition of firing. This suggests that intrinsic firing exhibited by Na^+-deficient NTS^{HSD2} neurons depends upon both $Na_v1.5$ and voltage-gated Ca^{2+} channels. We further investigated the interaction between $Na_v1.5$ and voltage-gated Ca^{2+} channels by testing the effect of QX-314 with the T-type Ca^{2+} channel blocker, TTA-A2, or the R-type Ca^{2+} channel blocker, SNX-482, on activity of NTS^{HSD2} neurons from Na^+-deprived mice. Neither TTA-A2 nor SNX-482 inhibited NTS^{HSD2} neuron firing when applied alone, as expected (Figure S5B). However, co-application of QX-314 and SNX-482, but not QX-314 and TTA-A2, markedly decreased AP firing resembling experiments with QX-314 and CCB (Figure 4I–J). Collectively, our results show that HCN channel conductance is permissive for spontaneous firing of NTS^{HSD2} neurons, and this HCN channel activity works in conjunction with Na^+ deficiency-induced increases in activity of $Na_v1.5$ and R-type Ca^{2+} channels to induce pacemaker-like activity.

NTS^{HSD2} Neurons are Necessary for Sodium Appetite

Since Na^+ deprivation activates NTS^{HSD2} neurons, we investigated their role in sodium appetite using *Hsd11b2-Cre* mice and AAV-FLEX-taCasp3-2A-TEVp-mediated genetic ablation (Figure 5A) (Yang et al., 2013). HSD2 immunofluorescence revealed that AAV-FLEX-taCasp3-2A-TEVp reduced the number of NTS^{HSD2} neurons by 65% compared with AAV-FLEX-GFP-injected controls (Figure 5B,C), but did not affect the number of nearby tyrosine hydroxylase (TH) neurons (Figure 5C). Thus, selective, partial ablation of NTS^{HSD2} neurons was achieved. Sodium appetite was assessed in Na^+-replete versus Na^+-deficient mice, the latter with or without NTS^{HSD2} neuron ablation. Mice were placed individually in lickometer cages equipped with two bottles; one filled with 3% NaCl and the other with H_2O. Furosemide diuresis markedly increased consumption of 3% NaCl in controls, while sodium appetite was mostly absent in mice lacking ~65% of their NTS^{HSD2} neurons (Figure 5D–F). Diminished 3% NaCl ingestion in ablated mice also lead to a small decrease in H_2O drinking compared to controls – a result also observed by others (Matsuda et al., 2017). In yet another model of Na^+ deficiency, we assessed sodium appetite in Na^+-deprived mice fed only low-sodium diet. However, unlike rats (Contreras and Hatton, 1975), chronic low-sodium diet alone does not significantly increase sodium appetite in mice (Rowland and Fregly, 1988). Therefore, we also H_2O-restricted the animals during the test to further increase hypovolemia and augment sodium appetite (see below). This protocol increased 3% NaCl drinking in control mice well above mice fed standard chow, but again NTS^{HSD2} neuron-ablated mice lacked Na^+ deprivation-induced appetite (Figure 5G–I). These results are consistent with a prior study using chemogenetic inhibition of NTS^{HSD2} neurons (Jarvie and Palmiter, 2017), and demonstrate the necessity of NTS^{HSD2} neurons for deficiency-induced sodium appetite.

Activation of NTS^{HSD2} Neurons Alone Does Not Rapidly Increase Sodium Appetite

We used a chemogenetic approach to selectively activate NTS^{HSD2} neurons (Krashes et al., 2011). AAV-DIO-hM3Dq-mCherry virus was injected into the NTS of *Hsd11b2-Cre* mice (Figure 6A) and we confirmed with HSD2 immunofluorescence that hM3Dq-mCherry was expressed selectively in NTS^{HSD2} neurons (Figure S6A–B). As expected, the hM3Dq ligand, clozapine-noxide (CNO), activated NTS^{HSD2} neurons as assessed by increased firing following CNO application to *ex vivo* brain slices (Figure 6B), and by induction of Fos following CNO injection (Figure 6C). Surprisingly, when chemogenetically activated in Na^+-replete mice, NTS^{HSD2} neurons did not increase sodium appetite in our 60-minute lickometer assay (Figure 6D). Thus, unlike Na^+ deficiency (Figure 5D–I), activation of NTS^{HSD2} neurons by themselves is insufficient to drive rapid sodium appetite.

Since Na^+ deficiency leads to a decrease in effective circulatory volume, it is possible that, in addition to regulating sodium appetite, NTS^{HSD2} neurons also regulate autonomic effector pathways to counter adverse cardiovascular consequences. They are well positioned to do this given their location in the NTS (Guyenet, 2006). Dual engagement of behavioral and physiologic effectors would be analogous to caloric deficiency-sensing AgRP neurons in the arcuate nucleus, which produce hunger and decreased energy expenditure when activated by either fasting or chemogenetic stimulation (Krashes et al., 2011). If deficiency-activated NTS^{HSD2} neurons behave similarly, then it is possible that intense chemogenetic stimulation

might produce extreme physiologic perturbations that could adversely affect behavior. To investigate this, we chemogenetically activated NTS^{HSD2} neurons and measured systolic and diastolic blood pressure in anesthetized mice (Figure S6C), as well as mean arterial pressure, heart rate, and locomotor activity via telemetry in the homecage of freely moving mice (Figure S6D–F). Importantly, chemogenetic activation produced no effect on blood pressure, heart rate or locomotor activity. Thus, NTS^{HSD2} neurons may not be analogous to deficiency-activated AgRP neurons, as they do not appear to coordinate autonomic regulation of cardiovascular function.

ATII Signaling Synergizes with NTS^{HSD2} Neurons to Induce Rapid Sodium Appetite

Given that both ATII and aldosterone signaling are important for inducing sodium appetite by the Na^+-deficient state (Matsuda et al., 2017; Sakai et al., 1986), and since NTS^{HSD2} neurons, by virtue of their activation by aldosterone, are the neuronal embodiment of the aldosterone signal, we hypothesized that isolated NTS^{HSD2} neuron stimulation fails to cause rapid appetite because ATII signaling is absent. In essence, increased ATII signaling could be a necessary precondition for rapid induction of sodium appetite by NTS^{HSD2} neurons. To test this, we sought to naturally elevate ATII coincident with NTS^{HSD2} neuron stimulation. This was accomplished by H_2O-restricting mice, which increases plasma ATII, but by itself does not greatly increase sodium appetite – presumably because aldosterone remains low and/or dehydration-induced hyperosmolarity inhibits salt appetite (Matsuda et al., 2017). Consistent with this, while H_2O restriction in the absence of NTS^{HSD2} neuron stimulation increased thirst, it did not significantly increase sodium appetite (euhydrated 3% NaCl licks − 75.8 ± 15.1; H_2O-restricted 3% NaCl licks − 124.3 ± 25; Paired t-test, P = 0.12). However, chemogenetic activation of NTS^{HSD2} neurons during H_2O restriction in the same mice now dramatically increased consumption of 3% NaCl (Figure 6E,F). The induced appetite was also specific for Na^+ because we failed to detect altered drinking behavior in H_2O-restricted mice when given a choice between 3% KCl and H_2O, but no access to 3% NaCl (Figure 6G). Finally, NTS^{HSD2} neuron stimulation in H_2O-restricted mice also increased consumption of a high-sodium diet (Figure S6G). As with liquid 3% NaCl, this did not occur when mice were euhydrated (Figure S6H). Consumption of standard chow, however, decreased with NTS^{HSD2} neuron stimulation in both euhydrated and dehydrated mice (Figure S6G–H). Decreased food intake with NTS^{HSD2} neuron stimulation was observed previously (Jarvie and Palmiter, 2017), and might relate to the phenomenon of Na^+ deficiency-induced anhedonia (Hurley and Johnson, 2015).

The ability of H_2O restriction to enable induction of sodium appetite by stimulating NTS^{HSD2} neurons could be due to ATII as we hypothesize, or alternatively, to some other aspect of dehydration – for example induction of thirst (i.e. the motivational drive to consume water). To confirm the role of ATII signaling, we validated that H_2O restriction elevated plasma ATII, and found the increase to be comparable to that of Na^+ depletion with furosemide (Figure 6H). Next, H_2O-restricted mice expressing hM3Dq in NTS^{HSD2} neurons were simultaneously injected with CNO and the AT1aR-specific blocker, losartan. Importantly, the addition of losartan completely prevented induction of sodium appetite in H_2O-restricted, NTS^{HSD2} neuron-stimulated mice (Figure 6I). Thus, ATII signaling is required for H_2O restriction to enable rapid appetite in NTS^{HSD2} neuron stimulated mice. To

examine the role of thirst *per se*, we created "ATII-independent" thirst in mice expressing hM3Dq in NTS^{HSD2} neurons. Hyperosmotic stimuli, such as those produced with peripheral injections of 1 M NaCl or 1 M sucrose, cause thirst by directly activating osmosensors (Fitzsimons, 1961; Zimmerman et al., 2016), and do not increase peripheral ATII (Abdelaal et al., 1976). While injection of either NaCl or sucrose markedly increased H_2O drinking, neither NaCl nor sucrose, unlike H_2O restriction, enabled increased consumption of 3% NaCl in response to NTS^{HSD2} neuron stimulation (Figure 6J,K). Finally, to directly test whether NTS^{HSD2} neurons and ATII signaling synergistically drive sodium appetite, we injected euhydrated mice expressing hM3Dq in NTS^{HSD2} neurons with both CNO and ATII. The combination of NTS^{HSD2} neuron activation and ATII administration greatly increased 3% NaCl licking unlike injection of either CNO or ATII alone (Figure 6L). Therefore, ATII signaling and not thirst *per se* enables rapid sodium appetite in NTS^{HSD2} neuron-stimulated mice.

At apparent odds with our above findings, it was recently shown, using a different method of assessing sodium appetite, that chemogenetic stimulation of NTS^{HSD2} neurons is sufficient to cause sodium appetite (Jarvie and Palmiter, 2017). These different conclusions between studies are presumably due to methodological difference(s). To rule out the possibility that differences in *Hsd11b2-Cre* knockin mice or chemogenetic tools explain the different results, we assessed sodium appetite using the protocol described by Jarvie and Palmiter. Specifically, while our approach above assessed appetite over 60 minutes during the day in naïve mice, their protocol involved prior experience with low-sodium diet and 3% NaCl before NTS^{HSD2} neuron stimulation tests, which were done at the onset of the dark cycle and lasted 4 hours. Adopting this approach, we found that NTS^{HSD2} neuron stimulation increased Na^+ consumption (Figure 7A–C), confirming their findings (Jarvie and Palmiter, 2017). Thus, it is the differences in protocols used to assess sodium appetite that account for the difference in conclusions regarding sufficiency of NTS^{HSD2} neuron stimulation. Of interest, in contrast to our earlier studies (Figure 6E), the sodium appetite induced by NTS^{HSD2} neuron stimulation under the conditions described by Jarvie and Palmiter was delayed in onset (Figure 7A,C). Little Na^+ consumption occurred during the first 30 minutes (Figure 7C). The reason for the delay is unclear as peripherally injected CNO activates hunger and thirst behaviors in hM3Dq-expressing AgRP or SFO neurons within minutes (Betley et al., 2015; Krashes et al., 2011). Consistent with rapid activation of hM3Dq-expressing neurons by CNO, Na^+ consumption induced by NTS^{HSD2} neuron stimulation in H_2O-restricted mice began to increase as soon as they were placed in the lickometer cage (Figure 6E).

We then investigated the hypothesis that the protocol used by Jarvie and Palmiter somehow increases ATII signaling and that this enables NTS^{HSD2} neuron stimulated sodium appetite. To accomplish this, we assessed plasma ATII levels and tested whether AT1aR antagonism could inhibit sodium appetite under these conditions. ATII measurements revealed that, unlike H_2O restriction, the protocol described by Jarvie and Palmiter does not increase plasma ATII (Figure 7D). Furthermore, simultaneously injected CNO and losartan did not block NTS^{HSD2} neuron-driven appetite (Figure 7E). These findings are interesting and suggest that, in the setting of their protocol, concurrent ATII signaling is not required for NTS^{HSD2} neuron induction of sodium appetite. In this context it is worth noting the

temporal differences in onset of sodium appetite with the two protocols (delayed in Figure 7A,C and rapid in Figure 6E). This raises the possibility that rapid induction of Na^+ ingestion by NTS^{HSD2} neuron stimulation (as in Figure 6E) requires ongoing ATII signaling.

NTS^{HSD2} Projections to the vlBNST Drive Sodium Appetite

To determine the downstream site mediating NTS^{HSD2} neuron-stimulated sodium appetite we mapped their projections by injecting AAV-DIO-synaptophysin (Syp1)-mCherry into the NTS of *Hsd11b2-Cre* mice (Figure S7). Consistent with previous reports (Geerling and Loewy, 2006a; Jarvie and Palmiter, 2017), NTS^{HSD2} neurons project heavily to a very focal subregion of the ventrolateral BNST (vlBNST) that also receives input from neurons expressing AgRP and calcitonin gene-related peptide (CGRP) (Figure S7C). In the brainstem, projections terminate in two distinct areas of the parabrachial complex (PB), a subregion in the central lateral parabrachial nucleus (LPBN), and in the pre-locus coeruleus (pLC). Interestingly, both regions are marked by neurons expressing FoxP2, which are activated by both Na^+ deficiency and chemogenetic stimulation of NTS^{HSD2} neurons (Geerling et al., 2011; Jarvie and Palmiter, 2017). Synaptic connectivity of NTS^{HSD2} neurons onto these downstream targets was next examined using *Hsd11b2-Cre* mice and CRACM (Figure 8A,B). Light-evoked excitatory postsynaptic currents (EPSCs) were detected in neurons residing within the NTS^{HSD2} neuron terminal field in the vlBNST (11 out of 13 neurons; 85%), pLC (13 out of 15 neurons; 87%), and LPBN (5 out of 15 neurons; 33%) (Figure 8C). Response latencies were ≤ 6 ms in all neurons indicative of monosynaptic connectivity. Finally, consistent with NTS^{HSD2} neurons expressing VGLUT2 (*Slc17a6*) (Figure 2B and Figure S3), light-evoked EPSCs were blocked by the glutamate receptor blocker, CNQX. Thus, NTS^{HSD2} neurons send strong glutamatergic projections to neurons in the vlBNST, pLC and LPBN.

Given the high connectivity to both vlBNST and PB (LPBN and nearby pLC), we tested whether optogenetic stimulation of NTS^{HSD2} axon terminals in either region drives sodium appetite. AAV-FLEX-ChR2 was injected into the NTS of *Hsd11b2-Cre* mice, and optic fibers were implanted bilaterally over the vlBNST or PB. Mice were H_2O-restricted as in previous chemogenetic experiments. Optical stimulation of ChR2-expressing terminals in the vlBNST, but not in the PB, induced rapid sodium appetite (Figure 8D–G). Thus, at least under H_2O-restricted conditions, NTS^{HSD2} neurons mediate their effects on sodium appetite through projections to the vlBNST. This finding is of particular interest as it was recently demonstrated that the same region, ventral BNST, is the target of sodium appetite-inducing, ATII receptor-expressing SFO neurons (Matsuda et al., 2017).

DISCUSSION

Deficiency of the major extracellular solute, Na^+, causes the effective circulatory volume to decrease. This is sensed by the periphery and brain, ultimately resulting in adaptive increases in both ATII and aldosterone (Eaton and Pooler, 2013). These hormones then correct the deficit in Na^+ by decreasing renal excretion and increasing ingestion of Na^+. Indeed, it was established many years ago that ATII and aldosterone each stimulate sodium appetite; when co-administered they synergistically increase appetite, and both are important

for induction of appetite by the Na^+-deficient state (Epstein, 1992; Matsuda et al., 2017; Sakai et al., 1986). While the mechanisms by which ATII and aldosterone regulate renal Na^+ excretion are fairly well understood (Arroyo et al., 2011; Eaton and Pooler, 2013), the brain mechanisms by which they induce sodium appetite are less well known. Very recently, two lines of investigation culminated in two important publications. It was shown that AT1aR-expressing SFO neurons that project to the ventral BNST (Matsuda et al., 2017) and NTS^{HSD2} neurons (Jarvie and Palmiter, 2017) both play important roles in driving sodium appetite. In the present study, we extend these observations by a) determining the electrophysiological mechanisms by which Na^+ deficiency activates NTS^{HSD2} neurons – uncovering unexpected roles for the cardiac pacemaking HCN and $Na_v1.5$ channels, by b) discovering that the aldosterone-sensing NTS^{HSD2} neurons interact with ATII signaling to induce appetite – thus providing a neuronal context for the ATII / aldosterone "synergy hypothesis" (Epstein, 1982; Fluharty and Epstein, 1983), and finally by c) establishing that the vlBNST is a downstream site by which NTS^{HSD2} neurons cause sodium appetite.

Cardiac Pacemaker Channels, HCN and $Na_v1.5$, Promote NTS^{HSD2} Neuron Firing

As assessed by Fos, NTS^{HSD2} neurons are activated by MR agonists and the Na^+-deficient state (Geerling et al., 2006; Geerling and Loewy, 2006b). Given that NTS^{HSD2} neurons are uniquely sensitive to aldosterone and that the aldosterone receptor is a nuclear transcription factor, we postulated that activation of NTS^{HSD2} neurons by Na^+ deficiency would occur independently of synaptic input. Consistent with this, using brain slice electrophysiology, we established that Na^+ deficiency *in vivo* induces intrinsic, "pacemaker-like" firing of synaptically isolated NTS^{HSD2} neurons. Prior studies have determined that such intrinsic activity of neurons is mediated by a complement of ion channels, for example those that bring resting membrane potential to a more depolarized state (i.e. NALCN and HCNs), and those that are activated at the higher subthreshold potentials ultimately leading to action potential firing (i.e. voltage-gated Na^+ and Ca^{2+} channels) (Khaliq and Bean, 2010). To determine which might be involved, we performed single-neuron RNA-Seq to identify channels expressed by NTS^{HSD2} neurons. This revealed remarkably high expression of two types of channels involved in cardiac pacemaking, HCN channels (*Hcn3* > *Hcn2* > *Hcn1* = *Hcn4*) and the TTX-resistant voltage-gated Na^+ channel, $Na_v1.5$ (*Scn5a*). By performing electrophysiology, we established that HCN and $Na_v1.5$ channels are indeed active in NTS^{HSD2} neurons, but not in randomly selected surrounding NTS neurons – thus they are a special property of NTS^{HSD2} neurons. Importantly, $Na_v1.5$ channel activity, but not HCN channel activity, is markedly induced by the Na^+-deficient state. The increase in $Na_v1.5$ channel activity may be caused by the over 3-fold increase in *Scn5a* gene expression, although this difference in expression did not meet our stringent criteria for statistical significance (False Discovery Rate = 0.13). In addition, aldosterone / MR signaling might increase $Na_v1.5$ activity through some cofactor that produces post-translational changes and/or enhanced trafficking to the plasma membrane – as occurs in the heart (Lou et al., 2016). Collectively, our results demonstrate that HCN channel activity is permissive for the pacemaker activity of NTS^{HSD2} neurons, and that induced $Na_v1.5$ and R-type Ca^{2+} channel activity collaborates with "background" HCN activity to bring about state-dependent pacemaker-like firing. Other channel activities are likely also involved including NALCN

leak current and subthreshold persistent activity (I_{NaP}) from other voltage-gated Na^+ channels.

NTS^{HSD2} neurons also abundantly express AT1aR. Consistent with this, their firing is markedly increased by exogenous application of ATII. As ATII is increased along with aldosterone during Na^+ deficiency, this could contribute meaningfully to their increased firing, *in vivo*, during Na^+ deficiency. In addition, the discovery of ATII activation of NTS^{HSD2} neurons may help to resolve the following paradox. While sodium appetite during Na^+ deficiency requires aldosterone signaling (Sakai et al., 1986), total deficiency of aldosterone and the subsequent renal wasting of Na^+ also causes intense sodium appetite. In agreement with a key role for aldosterone-activated NTS^{HSD2} neurons, paradoxically, they too are unexpectedly activated by Na^+ deprivation in the aldosterone-deficient state (Geerling et al., 2006). Given our finding that ATII activates NTS^{HSD2} neurons, high levels of ATII – induced by the renal Na^+ wasting and subsequent hypovolemia – could explain "paradoxical" activation of NTS^{HSD2} neurons in the aldosterone-deficient state.

Neuronal Context for ATII / Aldosterone Synergy in Driving Sodium Appetite

Thirty-five years ago Alan Epstein proposed the "synergy hypothesis" (Epstein, 1982; Fluharty and Epstein, 1983). Specifically, "*the brain is apprised of the need for salt, not by the deficiency itself, but by the endocrine consequences of deficiency, i.e. by concurrent elevations of both angiotensin* [ATII] *and aldosterone*" (Epstein, 1982). And "*sodium appetite may be aroused by a synergy of the peptide and the steroid*" (Fluharty and Epstein, 1983). Research over the years has confirmed the importance of both ATII and aldosterone for induction of appetite by Na^+ deficiency, and their synergistic ability to rapidly induce appetite in Na^+-replete animals (Epstein, 1992; Matsuda et al., 2017; Sakai et al., 1986). While much evidence supports the "synergy hypothesis", its neural basis has been unknown.

In this light, it is of interest that NTS^{HSD2} neurons, the neuronal embodiment of the aldosterone signal, are necessary but not sufficient for rapid induction of sodium appetite. Consistent with the "synergy hypothesis", such rapid induction requires concurrent ATII signaling. The key site(s) of ATII signaling is unknown, but AT1aR-expressing neurons in the SFO would seem to be likely candidates (Matsuda et al., 2017). Given that SFO neurons, like NTS^{HSD2} neurons, are also necessary for sodium appetite (Matsuda et al., 2017), this arrangement may protect against exaggerated Na^+ ingestion when it is not needed – e.g., elevations in aldosterone from hyperkalemia would be expected to stimulate NTS^{HSD2} neurons, but not SFO neurons, in the absence of Na^+ deficiency. Furthermore, it is unknown whether the required ATII signal originates in the periphery or in the brain. Given that the SFO is outside the blood-brain barrier and it is the primary candidate for ATII action, it seems likely that peripherally released ATII is the key signal. However, the relative role of peripheral versus central ATII has been a difficult issue for the field to resolve (Grobe et al., 2008). In the case of sodium appetite induced by the Na^+-deficient state, NTS^{HSD2} neurons could be another target for ATII action, as they too express AT1aRs and can be activated by ATII. However, this cannot account for ATII enabling sodium appetite in response to chemogenetic stimulation of NTS^{HSD2} neurons, as CNO/hM3Dq treatment bypasses any hypothetical activation by ATII. Finally, in a remarkable coincidence that likely has

mechanistic meaning, both AT1aR-expressing SFO neurons (Matsuda et al., 2017) and NTS^{HSD2} neurons (our study) drive sodium appetite via projections to the ventral BNST. This raises the distinct possibility that the ventral BNST is the key site where the ATII and aldosterone "neuronal signals" converge and synergistically generate sodium appetite. Future studies are required to address this important possibility.

STAR METHODS

CONTACT FOR REAGENT AND RESOURCE SHARING

Further information and requests for resources and reagents should be directed to and will be fulfilled by the Lead Contact, Bradford Lowell (blowell@bidmc.harvard.edu).

EXPERIMENTAL MODEL AND SUBJECT DETAILS

Mice—Prior to the start of experiments male mice were group housed in a temperature- and humidity-controlled room with a 12 hour light-dark cycle. These group housed animals had *ad libitum* access to standard chow (Envigo Teklad F6 8664; 0.3% sodium) and water. Unless otherwise specified male mice aged 8–12 weeks were single housed one week prior to experimental manipulation. In all experiments *Hsd11b2-Cre* (Naray-Fejes-Toth and Fejes-Toth, 2007), Ai9(lox)-tdTomato (Madisen et al., 2010), *Slc17a6*(VGLUT2)-*IRES-Cre* (Vong et al., 2011), *Slc32a1*(VGAT)-*IRES-Cre* (Vong et al., 2011), *Slc17a8*(VGLUT3)-*IRES-Cre* (Cheng et al., 2017), *Agrp-IRES-Cre* (Tong et al., 2008), and lox-L10-GFP (Krashes et al., 2014) mice were heterozygous for the transgene and maintained on a mixed background. All experiments were conducted in accordance with the guidelines of the Institutional Animal Care and Use Committee at Beth Israel Deaconess Medical Center.

METHOD DETAILS

Sodium deficiency and aldosterone experiments—Sodium deficiency for electrophysiological experiments was achieved via acute sodium depletion or chronic sodium deprivation. For sodium depletion (Figure 1B), male *Hsd11b2-Cre*::Ai9tdTomato mice aged 4–5 weeks were acclimated to single housing seven days prior to treatment with the loop diuretic furosemide (50 mg kg^{-1} ip) and then placed in a fresh cage with low-sodium diet (0.02% Na^+; Envigo TD.130591). The following day (16–24 hours post-injection) animals were sacrificed for NTS^{HSD2} neuron electrophysiology experiments. Sodium replete control animals received furosemide injections but continued to have access to standard chow (0.3% Na^+) in a fresh cage instead of low-sodium diet. In chronic dietary sodium deprivation experiments (Figure 1C,D & Figure S1), male *Hsd11b2-Cre*::Ai9tdTomato mice aged 4–5 weeks were given low-sodium diet or standard chow and fresh cages daily for 8–12 days prior to sacrifice for NTS^{HSD2} neuron electrophysiological recordings. In the case of chronic aldosterone infusion experiments (Figure 1F), osmotic minipumps (Alzet model 1002) containing vehicle (5% EtOH) or aldosterone (900 μg ml^{-1}) were placed in the abdominal cavity of male *Hsd11b2-Cre*::Ai9tdTomato mice aged 4–5 weeks. Mice were then individually housed with *ad libitum* access to water and standard chow for 8–12 days prior to electrophysiological recordings. The aldosterone concentration and duration of the minipump experiments were chosen to closely mimic the chronic sodium deprivation conditions used for NTS^{HSD2} neuron action potential firing experiments.

Hormone assays—To assess aldosterone levels of mice in sodium deficiency and aldosterone minipump experiments (Table S1), trunk blood was taken following sacrifice and centrifuged for serum collection. Serum was run in duplicate in a 96 well plate enzyme-linked immunosorbent assay (ELISA) kit for aldosterone (Alpco). Similarly, plasma angiotensin II was measured with an enzyme immunoassay (EIA; Peninsula Labs) kit from unrestrained mice under control, sodium-depleted (furosemide + LSD), and water-restricted condition (Figure 6H), as well as mice fed LSD with access to 3% NaCl and water (see chemogenetic drinking behavior experiments for specific experimental protocols). For the angiotensin II assay, trunk blood was collected in EDTA coated tubes upon sacrifice and centrifuged to obtain plasma. Protein was then extracted from the plasma using an acetone-based protocol (Kawashima et al., 2010). Extracted samples were dried using a vacuum centrifuge and dissolved in EIA buffer supplied in the kit. Measurements were carried out according to the manufacturer's protocol.

Electrophysiology—Animals were deeply anesthetized, decapitated and brains were quickly removed into ice-cold cutting solution consisting of (in mM): 72 sucrose, 83 NaCl, 2.5 KCl, 1 NaH_2PO4, 26 $NaHCO_3$, 22 glucose, 5 $MgCl_2$, 1 $CaCl_2$, oxygenated with 95% O_2/5% CO_2, measured osmolarity 310 – 320 mOsm/l. Cutting solution was prepared and used within 72 hours. 200- to 300-μm-thick coronal sections containing the NTS were cut with a vibratome and incubated in oxygenated cutting solution at 34 °C for 45 min. Slices were t ransferred to oxygenated aCSF (126 mM NaCl, 21.4 mM $NaHCO_3$, 2.5 mM KCl, 1.2 mM NaH_2PO_4, 1.2 mM $MgCl_2$, 2.4 mM CaCl2, 10 mM glucose) and stored in the same solution at room temperature (20–24 °C) for at least 60 min prior to recording. A single slice was placed in the recording chamber where it was continuously superfused at a rate of 3–4 ml per min with oxygenated aCSF. Neurons were visualized with an upright microscope equipped with infrared-differential interference contrast and fluorescence optics. Borosilicate glass microelectrodes (5–7 MΩ) were filled with internal solution. Experiments on HSD2 neurons were performed on brain slices from male *Hsd11b2-Cre*::Ai9tdTomato mice 5 to 7 weeks of age. NTS^{HSD2} neurons were identified by their tdTomato expression.

Whole-cell current-clamp recordings: Current-clamp recordings were performed with an intracellular solution containing (in mM): 128 potassium gluconate, 10 KCl, 10 HEPES, 1 EGTA, 1 $MgCl_2$, 0.3 $CaCl_2$, 5 Na_2-ATP, 0.3 Na-GTP (pH 7.3). Glutamatergic and GABAergic synaptic transmission was blocked by including CNQX (10 μM) and D-AP5 (50 μM) or kynurenate (1 mM) and picrotoxin (100 μm) or bicuculline (10 μM) ("synaptic blockers"), respectively, in the bath solution to synaptically isolate NTS^{HSD2} neurons. Action potential frequency was assessed for a period of 1 min immediately after breakthrough (Figure S1). Resting membrane potential (V_m) was determined in the presence of 1 μM TTX and synaptic blockers immediately after breakthrough (Figure 3C). Reported values of V_m were corrected for the liquid junction potential using the software Junction Potential Calculator (Clampex 10, Axon Instruments) and corrected offline. To test whether clozapine-n-oxide (CNO; 5 μM; Figure 6B) effectively caused increased activity it was bathed applied while recording from hM3Dq-expressing NTS^{HSD2} neurons.

Cell-attached recordings: Loose-seal, cell-attached recordings (seal resistance, 20–50 MΩ) were made in voltage clamp mode with aCSF as internal solution and holding current maintained at V_h = 0 mV. Synaptic blockers (see above) were included in the bath solution to synaptically isolate NTS^{HSD2} neurons. To test the effects of pharmacological agents on spontaneous AP firing, stable recordings were acquired for 3–5 min and aCSF solution containing the compound were perfused into the brain slice preparation. The following compounds were used in these experiments: aldosterone (100 nM; Figure 1E), angiotensin II (20 nM; Figure 1G,H), losartan (200 nM; Figure 1H), amiloride (100 μM; Figure S4C), CsCl (3 mM; Figure 3D), ZD7288 (50 μM; Figure 3E), TTA-A2 (10 μM; Figure 4I–J & Figure S5A–B), $CdCl_2$ (300 μM; Figure S5D,E), QX-314 chloride (1 mM; Figure 4G–J & Figure S5G), SNX-482 (300 nM; Figure 4I–J & Figure S5B), or a voltage-gated calcium channel blocker cocktail (Figure 4J & Figure S5F–G) containing nimodipine (10 μM), ω-conotoxin MVIIC (1 μM), SNX-482 (300 nM), and TTA-A2 (10 μM).

I_h current recordings: I_h currents (Figure 3A,B) were recorded in presence of (in mM): 0.001 TTX, 1 kynurenic acid, 0.1 picrotoxin, 1 barium chloride, 0.1 $NiCl_2$. To determine the voltage sensitivity of I_h activation, cells were held at −50 mV and 10 mV voltage steps were applied from −50 to −120 mV (5 or 10 s, 10 mV/step). The amplitude of I_h was then determined by measuring the difference in the instantaneous and steady-state currents achieved at the beginning and end of the pulse, respectively.

Evoked low-voltage activated currents: Whole-cell voltage-clamp recordings of currents (Figure 4A–F & Figure S5A,C) were performed with an intracellular solution containing (in mM):140 CsCl, 1 BAPTA, 10 HEPES, 5 $MgCl_2$, 5 Mg-ATP, and 0.3 Na_2GTP (pH 7.3; osmolarity, 290 mOsm). The following compounds were included in the bath (in mM): 1 tetraethylammonium chloride, 1 4-aminopyridine, 3 CsCl, 1 kynurenic acid, 0.1 picrotoxin. NTS^{HSD2} neurons were held at −70 mV. After a 1 second hyperpolarization step to −100 mV, low voltage activated inward currents were evoked by step depolarization to −50 mV for 200 ms every 20 seconds.

Channelrhodopsin-2 circuit mapping (CRACM): For CRACM experiments (Figure 8C) male mice aged 7–10 weeks were deeply anesthetized, decapitated and brains were quickly removed into an ice-cold NMDG-based cutting solution containing (in mM): 93 NMDG, 2.5 KCl, 1.2 NaH2PO4, 30 NaHCO3, 20 HEPES, 25 glucose, 5 sodium ascorbate, 2 thiourea, 3 sodium pyruvate, 10 MgSO4, 0.5 CaCl2 (pH 7.3 adjusted with HCl; oxygenated with 95% O2, 5% CO2; 310–320 mOsm). 300-μm-thick coronal sections from NTS^{HSD2} neuron projection sites (See Figure S7 & Figure 8C) were cut with a vibratome and incubated in NMDG-based cutting solution at 34 °C for 10 min. Slices were transferr ed to oxygenated aCSF and recovered for 30 min at 34 °C. Slices were stored in oxygenated aCSF at room temperature (20–24 °C) for at least 60 min before recording. Whole-cell voltage clamp recordings were obtained using a Cs-based internal solution containing (in mM): 135 CsMeSO3, 10 HEPES, 1 EGTA, 4 MgCl2, 4 Na2-ATP, 0.4 Na2-GTP, 10 Na_2-phosphocreatine (pH 7.3; 295 mOsm). Light-evoked EPSCs were recorded in whole-cell voltage-clamp mode, with membrane potential clamped at V_h = −70 mV. Bicuculline or picrotoxin was included in the bath to isolate glutamatergic currents. To photostimulate

ChR2-positive fibers, a laser or LED light source (473 nm) was used. The blue light was focused onto the back aperture of the microscope objective, producing wide-field exposure around the recorded cell of 10–15 mW per mm^2 as measured using an optical power meter (PM100D, Thorlabs). The light output was controlled by a programmable pulse stimulator, Master-8 (A.M.P.I.) and pClamp 10.2 software (Axon Instruments). The light-evoked EPSC detection protocol consisted of four blue light pulses (473 nm wavelength, 5 msec) administered 1 s apart during the first 4 s of an 8-s sweep, repeated for a total of 30 sweeps. Evoked EPSCs with short latency (≤6 ms) upon light stimulation were considered as light-driven (Krashes et al., 2014).

Analysis: All recordings were made using a Multiclamp 700B amplifier, and data were filtered at 2 kHz and digitized at 10 or 20 kHz. Access resistance (<30 MΩ) was continuously monitored by a voltage step and recordings were accepted for analysis if changes were <15%. All recordings were analyzed offline using Clampfit 10.

Single cell RNA sequencing—Cells were manually isolated for single-cell RNA-Seq (Figure 2 & Figure S4) as previously described (Campbell et al., 2017). Briefly, after rapid decapitation of male *Hsd11b2-Cre*::Ai9tdTomato mice aged 5–6 weeks, a brain matrix was used to make fresh 1mm-thick brainstem slices. The fluorescent signal from tdTomato+ neurons was used to visually guide microdissection of the NTS, which was then digested with papain for 1hr at 37° C, washed, and then dissociated by triturating with a series of fire-polished Pasteur pipettes. The cell suspension was washed and plated, and individual tdTomato+ NTS cells were collected by micropipette, washed, and frozen at −80 °C. Frozen cells were later lysed for poly dT-primed reverse transcription and 25 cycles of PCR amplification with SmartSeq2 (Picelli et al., 2014). To control for mRNA contamination during cell picking, an equivalent volume of cell-picking buffer was sampled and processed with each batch of cells. Amplified cDNA was analyzed for expression of the housekeeping gene *Actb* by quantitative PCR (qPCR) (Integrated DNA Technologies). Single-cell samples that exhibited an *Actb* C_t value greater than 30 cycles were excluded, as were sample batches in which the cell-picking buffer showed evidence of mRNA contamination. Barcoded RNA-Seq libraries were constructed with a commercially available kit (Nextera XT DNA Library Prep Kit) and sequenced in multiplex by Illumina NextSeq (75-base single-end reads). Pass-filter reads were aligned to the mouse mm10 genome by HiSAT2 (Goldstein et al., 2016; Kim et al., 2015). PCR duplicates were filtered using the MarkDuplicates program in the Picard toolkit (http://broadinstitute.github.io/picard/faq.html). Aligned reads were quantified with featureCounts software (Liao et al., 2014) in units of CPM (Counts per million). To exclude cells that only expressed Hsd11b2 during development (but were permanently labeled by tdTomato expression), we calculated an expression cutoff for Hsd11b2 using a published formula (Usoskin et al., 2015) and filtered out any cells that expressed Hsd11b2 below this cutoff. Furthermore, cells with library size of < 50,000 counts were excluded from further analysis.

RNA sequencing differential expression analysis: Pairwise differential analysis between the NTS^{HSD2} neurons from standard chow (Chow)- and low-sodium diet (LSD)-fed mice was performed using the Bioconductor package edgeR. First we normalized counts based on

library size to arrive at Counts Per Million (CPM) values. These CPM values were transformed into log space by adding a small constant (scaled by library size and centered at 0.25) to avoid taking the log of 0 and then taking the log base 2. Only genes that were not expressed at >4 $\log^2$ (CPM) in at least 5 cells were filtered out of the differential expression analysis. Genes with a log2 fold change between the two conditions > 1 and a False Discovery Rate (FDR) < 0.05 were considered significant.

Stereotaxic surgery and viral injections—For viral injections into the NTS, five- to eight-week-old male mice were anesthetized with a ketamine (100 mg kg^{-1}) and xylazine (10 mg kg^{-1}) cocktail diluted in 0.9% saline and placed into a stereotaxic apparatus (David Kopf model 940) with the head angled down at approximately 45°. An incision was made at the level of the ciste rna magna, then skin and muscle was retracted to expose the dura mater covering the 4th ventricle. A 28-gauge needle was used to make an incision in the dura and allow access to the brainstem. A pulled glass micropipette (20–40 μm diameter tip) was used for stereotaxic injections of adeno-associated virus (AAV), and coordinates for NTS injections were anterior 0.3 mm, lateral ± 0.15 mm, and ventral 0.3 mm from calamus scriptorius. Virus was injected (200 nl/side) by an air pressure system using picoliter air puffs through a solenoid valve (Clippard EV 24VDC) pulsed by a Grass S48 stimulator to control injection speed (40 nl min^{-1}). The pipette was removed 3 minutes post-injection followed by wound closure using absorbable suture for muscle and silk suture for skin. Subcutaneous injection of sustained release Meloxicam (4 mg kg^{-1}) was provided as postoperative care. AAV1-EF1α-FLEX-taCasp3-TEVp and AAV8-hSyn-FLEX-eGFP were used for selective ablation studies (Figure 5) and purchased from the University of North Carolina (UNC) Vector Core (donating investigators, Dr. Nirao Shah and Dr. Bryan Roth, respectively). Chemogenetic experiments (Figure 6, Figure 7, & Figure S6) utilized AAV8-hSyn-DIO-hM3Dq-mCherry purchased from the UNC Vector Core (donating investigator, Dr. Bryan Roth). Anterograde tracing (Figure S7) was done using AAV8-Ef1a-DIO-synaptophysin(Syp1)-mCherry developed by Dr. Rachel Neve at the Massachusetts Institute of Technology McGovern Institute for Brain Research Viral Vector Core and purchased from Virovek, Inc. Finally, optogenetic studies (Figure 8) were done using AAV9-EF1α-DIO-ChR2(H134R)-eYFP purchased from the University of Pennsylvania School of Medicine Vector Core (donating investigator, Dr. Karl Deisseroth). Animals were allowed to recover from stereotaxic surgery a minimum of 14 days prior to initiation of any experiments. Following each experimental procedure, accuracy of AAV injections was confirmed via post-hoc histological analysis of mCherry or YFP fluorescent protein reporters. All subjects determined to be surgical "misses" based on little or absent reporter expression were removed from analyses.

Jugular-Nodose ganglia complex AAV injections: AAV injection of nodose ganglia (Figure S2) was done as previously described (Chang et al., 2015). Briefly, the left nodose/jugular complex was exposed by making an incision along the ventral surface of the neck and blunt dissection. AAV9-CAG-ChR2-GFP was purchased from the UNC Vector Core (donating investigator, Dr. Edward Boyden) and injected (140 nl) using a Nanoject II injector (Drummond). Animals recovered from surgery and were sacrificed 3 weeks later at 8 weeks of age for electrophysiological recordings.

Optic fiber implantation: For *in vivo* behavioral optogenetics (Figure 8D–G), optic fibers (200 μm diameter core; Thor Labs) were implanted bilaterally over the projection sites of NTS^{HSD2} neurons. Stereotaxic coordinates for vlBNST fibers from bregma were anterior +0.1 mm, lateral ± 1.0 mm, and ventral −4.4 mm, while PB coordinates from bregma were posterior −5.3 mm, lateral ± 1.3 mm, and ventral −3.0 mm. Fibers were fixed to the skull using dental acrylic and mice were allowed to recover 14 days prior to the start of acclimation to behavioral testing.

Sodium appetite behavioral studies—Sodium appetite was assessed using two-bottle Drinking Event Monitor cages (Lickometer cages; Columbus Instruments). Individual male mice aged 8–16 weeks were placed into these "lickometer" cages where licks on each bottle sipper tube were detected by electrical conductivity and recorded by a computer counter interface. Each lick was calculated to equal approximately 2.2 μl ± 0.3 μl in volume by taking the change in weight of the water bottles after drinking sessions and dividing by the total amount of licks registered. Initially for training and acclamation, mice were H_2O-deprived overnight and the next day placed into Drinking Event Monitor cages with free access to one bottle containing H_2O and another containing 3% NaCl for a one-hour session. Training sessions were considered a success if both bottles registered licks and the mice accumulated ≥ 200 licks combined during the test. For H_2O restriction experiments, H_2O continued to be withheld from the home cage after training, and animals had free access to H_2O and 3% NaCl during daily lickometer tests lasting at least an hour. During H_2O restriction studies, body weight and signs of dehydration were monitored daily to ensure health.

Sodium deficiency-induced sodium appetite: Sodium deficiency for behavioral experiments was achieved via acute sodium depletion or chronic sodium deprivation similar to electrophysiology experiments. For sodium depletion (Figure 5D–F), male *Hsd11b2-Cre* mice aged 7–12 weeks were treated with furosemide (50 mg kg^{-1} ip) and then placed in a fresh cage with low-sodium diet. The following day sodium appetite behavior was evaluated. Furosemide control animals received furosemide injections but continued to have access to standard chow in a fresh cage instead of low-sodium diet. For induction of sodium appetite by chronic dietary sodium deprivation (Figure 5G–I), male *Hsd11b2-Cre* mice aged 7–12 weeks were maintained on LSD for 15–21 days and were also restricted to one-hour access to H_2O in the final 3 days to facilitate sodium ingestion in the one-hour test. Lickometer training occurred on the 2 days prior to the two-bottle choice test with only the H_2O bottle in place.

Chemogenetic drinking behavior experiments: Male *Hsd11b2-Cre* mice aged 8–16 weeks expressing hM3Dq-mCherry in NTS^{HSD2} neurons were injected intraperitoneally (ip) with either vehicle or clozapine-n-oxide (CNO; 1 mg kg^{-1}; 0.5% body weight volume) 10 minutes prior to being placed into the Drinking Event Monitor cage (Figure 6D–G,I). To avoid supplying mice with sodium in these injections, CNO was delivered in 1% DMSO. In angiotensin receptor antagonist experiments (Figure 6I), H_2O-restricted mice were co-injected with losartan (20 mg kg^{-1}) and either vehicle or CNO 15 minutes prior to being placed in to the Drinking Event Monitor cage. For hyperosmotic manipulations causing

motivation to drink water (Figure 6J,K), animals were injected ip with a 2% body weight volume of 1 M NaCl or 1 M Sucrose (Sigma) and either vehicle or CNO, then immediately placed in the Drinking Event Monitor cage for testing. In ATII synergy experiments (Figure 6L), mice were first injected ip with either vehicle or CNO and placed back into their homecage for 10 minutes. Then mice were again removed from their homecage, injected with angiotensin II subcutaneously (0.25 mg kg^{-1} in a 0.5% body weight volume; Sigma), and placed in the lickometer box for testing. Vehicle/Vehicle, CNO/Vehicle, Vehicle/ATII, and CNO/ATII injections were counterbalanced to avoid order effects. For experiments related to Figure 7A–E, behavioral testing was performed as described by Jarvie and Palmiter (2017). Briefly, animals were continually housed in modified Drinking Event Monitor cages with free access to low-sodium diet, 3% NaCl, and H_2O. Mice were given an acclimation period of at least three days prior to the start of behavioral testing. Following acclimation, mice received vehicle injections for another three days prior to CNO/hM3Dq stimulation of NTS^{HSD2} neurons to establish baseline 3% NaCl and H_2O drinking behavior. Injections of vehicle or CNO were done 30 minutes prior to the onset of dark and behavioral data reported are from the first four hours of the dark-cycle. In angiotensin receptor antagonist experiments (Figure 7E), losartan (20 mg kg^{-1}) with either vehicle or CNO was injected in the same manner. For plasma angiotensin II measurements under these conditions, trunk blood was taken one-hour into the dark cycle.

Chemogenetic feeding behavior experiments: For sodium appetite feeding studies (Figure S6G,H), male *Hsd11b2-Cre* mice aged 8–16 weeks were acclimated to a two-diet choice of high sodium diet (1.6% Na^+ / 4% NaCl; Envigo TD.92034) or standard diet (0.2% Na^+ / 0.49% NaCl; Envigo TD.96208) for at least 5 days before commencing food intake experiments in the home cage. Because the high sodium diet formulation differed slightly from our in-house standard chow, these experiments used the appropriate control diet matching its formulation offered by the manufacturer. For dark-cycle feeding experiments, the two diets were pre-weighed and male *Hsd11b2-Cre* mice received a vehicle or CNO injection approximately 10 minutes prior to the onset of dark. Food was again weighed each hour for the next 3 hours and the remaining food weight values were subtracted from the initial pre-weighed food to provide the amount eaten. In water restriction experiments, animals had *ad libitum* access to high sodium and standard diets and were acclimated to three-hour restricted H_2O access (11:00 – 14:00) for two days prior to the experiment. Next, diets were pre-weighed and animals received vehicle or CNO injections 10 minutes prior to H_2O access. Food intake was measured for the next three hours.

Optogenetic behavioral experiments: For optogenetic terminal stimulation experiments (Figure 8D–G), modified two-bottle Drinking Event Monitor cages were used to accommodate the optogenetic equipment. Similar to chemogenetic studies, male *Hsd11b2-Cre* mice aged 8–16 weeks were H_2O-restricted prior to a two-bottle choice test. Fiber optic cables (1.0 m length, 200 mm diameter; Doric Lenses) were firmly attached to fiber optic ferrules with zirconia sleeves (Doric Lenses). Light pulse trains (10 ms pulses of 20 Hz; 1 second on, 3 seconds off) were programmed using a waveform generator (National Instruments) that provided TTL input to a blue light LED (465 nm; Plexon). Optogenetic stimulation began 2 minutes prior to access to 3% NaCl or H_2O and upon bottle placement

behavioral sessions lasted for 20 minutes. Post-stimulation, animals were allowed *ad libitum* access to H2O and 3% NaCl for at least another 40 minutes. The light power exiting the fiber optic cable measured by an optical power meter was 6–8 mW in all experiments. After completion of photostimulation experiments, mice were perfused for assessment of surgical accuracy of ChR2 expression and optic fiber tip location via histological analysis.

Blood pressure experiments—Anesthetized blood pressure recordings in 10-week-old male *Hsd11b2-Cre* mice expressing hM3Dq in NTS^{HSD2} neurons (Figure S6C) were performed under isoflurane anesthesia. The carotid artery was isolated and cannulated with a 1.4-Fr (SPR-671) high-fidelity microtip transducer catheter connected to a data acquisition system (PowerLab ML820, ADInstrument, Colorado Springs) through a pressure interface unit (Millar Instrument, Transducer Balance, TCB 600). After establishing a 15-minute, stable baseline mice were injected i.p. first with vehicle and recordings continued for 30 minutes. Next, CNO was administered and recordings continued for another 30 minutes. Finally, animals were sacrificed for histological verification of hM3Dq-mCherry expression in NTS^{HSD2} neurons. The blood pressure data were collected and analyzed using LabChart software.

Blood pressure telemetry: Direct blood pressure monitoring (Figure S6D–F) was done using radiotelemetry (Data Sciences International; DSI). Surgical implantation of HD-X11 transmitters was performed in 10-week-old male *Hsd11b2-Cre* mice expressing hM3Dq in NTS^{HSD2} neurons via left common carotid artery occlusion under isoflurane anesthesia with meloxicam (5mg/Kg, s.c.) as analgesic. Following surgical site preparation, a 1 cm midline incision was made on the ventral surface from the sternal notch rostrally. The subcutaneous tissues and salivary glands within the neck were bluntly dissected and the left carotid sheath was exposed. The left common carotid artery was dissected from the carotid sheath, then a small vascular clamp was placed proximally and an occluding suture was tied distally. The artery was then punctured with a 25G needle, which guides the tip of the catheter. The needle and vascular clamp were removed. The catheter was carefully advanced through the artery and sutured into place. The body of the transmitter was placed into a subcutaneous pocket on the right flank. The incision was sutured and the mouse monitored until recovering spontaneous locomotion. We allowed a 7–10 day recovery period before experimental recordings. Data Acquisition was through DataQuest A.R.T. (DSI), which was set to record every 10 seconds, 24h/day. Vehicle or CNO was injected three hours into the light-cycle. Vehicle and CNO injections were repeated two times in reverse order (Veh; CNO; CNO; Veh) and results averaged. Data for each animal was exported into Excel for analysis.

Histology—Mice were terminally anesthetized with 7% choral hydrate (500 mg kg^{-1}; Sigma Aldrich) diluted in saline and transcardially perfused first with 0.1 M phosphate-buffered saline (PBS) then 10% neutral-buffered formalin solution (NBF; Thermo Fisher Scientific). Brains were extracted and post-fixed overnight at 4° C in NBF. The next day b rains were switched to PBS containing 20% sucrose for cryoprotection. Finally, brains were sectioned coronally at 30 μm on a freezing microtome (Leica Biosystems), and stored in cryoprotectant solution at −20° C until used for immunofluorescence.

Immunofluorescence: Brain tissue sections were washed 3X in PBS prior to a blocking step containing 3% normal donkey serum and 0.4% Triton X-100 in PBS for one hour at room temperature. Primary antibody was prepared in the same blocking solution and incubated overnight at the following concentrations: Rabbit anti-HSD2 (H-145; Santa Cruz Biotechnology) 1:300, Rabbit anti-TH (EMD Millipore) 1:3,000, Rat anti-mCherry (Life Technologies) 1:3,000, Chicken anti-GFP (Life Technologies) 1:3,000, Rabbit anti- c-Fos (EMD Millipore) 1:3,000, Rabbit anti-CGRP (Peninsula Labs) 1:1,000, Goat anti-AgRP (Neuromics) 1:3,000, and Sheep anti-FoxP2 (R&D Systems) 1:1,000. The next day sections were washed 5X in PBS, then incubated for 2 hours at room temperature in Alexa Fluor fluorescent secondary antibody (Life Technologies; 1:1,000) prepared in blocking solution. Finally, sections were washed 3X in PBS, mounted on gelatin-coated slides, and coverslipped with Vectashield mounting media containing DAPI (Vector Labs). Fluorescent images were captured using an Olympus VS120 slide-scanning microscope. In NTS^{HSD2} neuron ablation experiments (Figure 5B,C), one of three serial sections was used for posthoc histological analysis of HSD2 and TH immunoreactive neurons.

QUANTIFICATION AND STATISTICAL ANALYSIS

Statistical analyses were performed using Prism 7 (GraphPad) software and are described in the figure legends in all cases except for RNA sequencing data where detailed analysis is described above. No statistical method was used to predetermine sample size, nor were randomization and blinding methods used and statistical significance was defined as $P < 0.05$. All data presented met the assumptions of the statistical test employed. As mentioned earlier, experimental animals were excluded if histological validation revealed poor or absent reporter expression and this was established prior to data collection. N values reflect the final number of validated animals per group.

DATA AND SOFTWARE AVAILABILITY

RNA-Seq data are available at Gene Expression Omnibus (GEO), accession code GSE102332. All other relevant data supporting the findings of this study are available from the lead contact upon reasonable request.

Supplementary Material

Refer to Web version on PubMed Central for supplementary material.

Acknowledgments

We would like to thank: Dr. B. Bean for advice regarding electrophysiology experiments and pacemaker neurons. Drs. S. Liberles and D. Strochlic for helpful discussions and technical assistance regarding nodose ganglia experiments. Drs. M. Zeidel, M. Andermann, and the Lowell laboratory for helpful discussions. C. Jacobs and the BNORC Functional Genomics and Bioinformatics core for helpful discussions and technical assistance. Y. Li, Z. Yang, and J. Yu for technical assistance. The BIDMC Molecular Medicine Core for technical assistance. This research was funded by the following NIH grants to B.B.L.: R01 DK075632, R01 DK096010, R01 DK089044, R01 DK111401, P30 DK046200, P30 DK057521; to J.C.G.: K08 NS099425; to J.M.R.: F32 DK103387. J.N.C. was supported by an AHA Postdoctoral Fellowship (14POST20100011), and Y.L. was supported by an EMBO postdoctoral fellowship.

References

Abdelaal AE, Mercer PF, Mogenson GJ. Plasma angiotensin II levels and water intake following beta-adrenergic stimulation, hypovolemia, cellular dehydration and water deprivation. Pharmacol Biochem Behav. 1976; 4:317–321. [PubMed: 6974]

Arroyo JP, Ronzaud C, Lagnaz D, Staub O, Gamba G. Aldosterone paradox: differential regulation of ion transport in distal nephron. Physiology (Bethesda). 2011; 26:115–123. [PubMed: 21487030]

Betley JN, Xu S, Cao ZF, Gong R, Magnus CJ, Yu Y, Sternson SM. Neurons for hunger and thirst transmit a negative-valence teaching signal. Nature. 2015; 521:180–185. [PubMed: 25915020]

Campbell JN, Macosko EZ, Fenselau H, Pers TH, Lyubetskaya A, Tenen D, Goldman M, Verstegen AM, Resch JM, McCarroll SA, et al. A molecular census of arcuate hypothalamus and median eminence cell types. Nat Neurosci. 2017; 20:484–496. [PubMed: 28166221]

Chang RB, Strochlic DE, Williams EK, Umans BD, Liberles SD. Vagal Sensory Neuron Subtypes that Differentially Control Breathing. Cell. 2015; 161:622–633. [PubMed: 25892222]

Cheng L, Duan B, Huang T, Zhang Y, Chen Y, Britz O, Garcia-Campmany L, Ren X, Vong L, Lowell BB, et al. Identification of spinal circuits involved in touch-evoked dynamic mechanical pain. Nat Neurosci. 2017; 20:804–814. [PubMed: 28436981]

Contreras RJ, Hatton GI. Gustatory adaptation as an explanation for dietary-induced sodium appetite. Physiology & Behavior. 1975; 15:505–633.

Dreyfus FM, Tscherter A, Errington AC, Renger JJ, Shin HS, Uebele VN, Crunelli V, Lambert RC, Leresche N. Selective T-type calcium channel block in thalamic neurons reveals channel redundancy and physiological impact of I(T)window. J Neurosci. 2010; 30:99–109. [PubMed: 20053892]

Eaton, DC., Pooler, JP. Vander's Renal Physiology. Eighth. McGraw-Hill Education; 2013.

Epstein AN. Mineralocorticoids and cerebral angiotensin may act together to produce sodium appetite. Peptides. 1982; 3:493–494. [PubMed: 7122274]

Epstein AN. Control of salt intake by steroids and cerebral peptides. Pharmacol Res. 1992; 25:113–124.

Fitzsimons JT. Drinking by nephrectomized rats injected with various substances. J Physiol. 1961; 155:563–579. [PubMed: 13700080]

Fluharty SJ, Epstein AN. Sodium appetite elicited by intracerebroventricular infusion of angiotensin II in the rat: II. Synergistic interaction with systemic mineralocorticoids. Behav Neurosci. 1983; 97:746–758. [PubMed: 6639747]

Fox AP, Nowycky MC, Tsien RW. Kinetic and pharmacological properties distinguishing three types of calcium currents in chick sensory neurones. J Physiol. 1987; 394:149–172. [PubMed: 2451016]

Frelin C, Cognard C, Vigne P, Lazdunski M. Tetrodotoxin-sensitive and tetrodotoxin-resistant Na+ channels differ in their sensitivity to Cd2+ and Zn2+ Eur J Pharmacol. 1986; 122:245–250. [PubMed: 2423344]

Frenz CT, Hansen A, Dupuis ND, Shultz N, Levinson SR, Finger TE, Dionne VE. NaV1.5 sodium channel window currents contribute to spontaneous firing in olfactory sensory neurons. J Neurophysiol. 2014; 112:1091–1104. [PubMed: 24872539]

Fu XW, Brezden BL, Wu SH. Hyperpolarization-activated inward current in neurons of the rat's dorsal nucleus of the lateral lemniscus in vitro. J Neurophysiol. 1997; 78:2235–2245. [PubMed: 9356377]

Fu Y, Vallon V. Mineralocorticoid-induced sodium appetite and renal salt retention: evidence for common signaling and effector mechanisms. Nephron Physiol. 2014; 128:8–16. [PubMed: 25376899]

Geerling JC, Engeland WC, Kawata M, Loewy AD. Aldosterone target neurons in the nucleus tractus solitarius drive sodium appetite. J Neurosci. 2006; 26:411–417. [PubMed: 16407537]

Geerling JC, Loewy AD. Aldosterone-sensitive neurons in the nucleus of the solitary: efferent projections. J Comp Neurol. 2006a; 498:223–250. [PubMed: 16933386]

Geerling JC, Loewy AD. Aldosterone-sensitive NTS neurons are inhibited by saline ingestion during chronic mineralocorticoid treatment. Brain Res. 2006b; 1115:54–64. [PubMed: 16935272]

Geerling JC, Stein MK, Miller RL, Shin JW, Gray PA, Loewy AD. FoxP2 expression defines dorsolateral pontine neurons activated by sodium deprivation. Brain Res. 2011; 1375:19–27. [PubMed: 21108936]

Goldin AL. Resurgence of sodium channel research. Annu Rev Physiol. 2001; 63:871–894. [PubMed: 11181979]

Goldstein LD, Cao Y, Pau G, Lawrence M, Wu TD, Seshagiri S, Gentleman R. Prediction and Quantification of Splice Events from RNA-Seq Data. PLoS One. 2016; 11:e0156132. [PubMed: 27218464]

Grobe JL, Xu D, Sigmund CD. An intracellular renin-angiotensin system in neurons: fact, hypothesis, or fantasy. Physiology (Bethesda). 2008; 23:187–193. [PubMed: 18697992]

Guyenet PG. The sympathetic control of blood pressure. Nat Rev Neurosci. 2006; 7:335–346. [PubMed: 16760914]

Hadchouel J, Ellison DH, Gamba G. Regulation of Renal Electrolyte Transport by WNK and SPAK-OSR1 Kinases. Annu Rev Physiol. 2016; 78:367–389. [PubMed: 26863326]

Henry FE, Sugino K, Tozer A, Branco T, Sternson SM. Cell type-specific transcriptomics of hypothalamic energy-sensing neuron responses to weight-loss. Elife. 2015; 4

Hurley SW, Johnson AK. The biopsychology of salt hunger and sodium deficiency. Pflugers Arch. 2015; 467:445–456. [PubMed: 25572931]

Jarvie BC, Palmiter RD. HSD2 neurons in the hindbrain drive sodium appetite. Nat Neurosci. 2017; 20:167–169. [PubMed: 27918529]

Kawashima Y, Fukutomi T, Tomonaga T, Takahashi H, Nomura F, Maeda T, Kodera Y. High-yield peptide-extraction method for the discovery of subnanomolar biomarkers from small serum samples. J Proteome Res. 2010; 9:1694–1705. [PubMed: 20184378]

Khaliq ZM, Bean BP. Pacemaking in dopaminergic ventral tegmental area neurons: depolarizing drive from background and voltage-dependent sodium conductances. J Neurosci. 2010; 30:7401–7413. [PubMed: 20505107]

Kim D, Langmead B, Salzberg SL. HISAT: a fast spliced aligner with low memory requirements. Nat Methods. 2015; 12:357–360. [PubMed: 25751142]

Krashes MJ, Koda S, Ye C, Rogan SC, Adams AC, Cusher DS, Maratos-Flier E, Roth BL, Lowell BB. Rapid, reversible activation of AgRP neurons drives feeding behavior in mice. J Clin Invest. 2011; 121:1424–1428. [PubMed: 21364278]

Krashes MJ, Shah BP, Madara JC, Olson DP, Strochlic DE, Garfield AS, Vong L, Pei H, Watabe-Uchida M, Uchida N, et al. An excitatory paraventricular nucleus to AgRP neuron circuit that drives hunger. Nature. 2014; 507:238–242. [PubMed: 24487620]

Lei M, Zhang H, Grace AA, Huang CL. SCN5A and sinoatrial node pacemaker function. Cardiovasc Res. 2007; 74:356–365. [PubMed: 17368591]

Liao Y, Smyth GK, Shi W. featureCounts: an efficient general purpose program for assigning sequence reads to genomic features. Bioinformatics. 2014; 30:923–930. [PubMed: 24227677]

Lou Y, Zhang F, Luo Y, Wang L, Huang S, Jin F. Serum and Glucocorticoid Regulated Kinase 1 in Sodium Homeostasis. Int J Mol Sci. 2016; 17

Madisen L, Zwingman TA, Sunkin SM, Oh SW, Zariwala HA, Gu H, Ng LL, Palmiter RD, Hawrylycz MJ, Jones AR, et al. A robust and high-throughput Cre reporting and characterization system for the whole mouse brain. Nat Neurosci. 2010; 13:133–140. [PubMed: 20023653]

Matsuda T, Hiyama TY, Niimura F, Matsusaka T, Fukamizu A, Kobayashi K, Kobayashi K, Noda M. Distinct neural mechanisms for the control of thirst and salt appetite in the subfornical organ. Nat Neurosci. 2017; 20:230–241. [PubMed: 27991901]

Naray-Fejes-Toth A, Colombowala IK, Fejes-Toth G. The role of 11beta-hydroxysteroid dehydrogenase in steroid hormone specificity. J Steroid Biochem Mol Biol. 1998; 65:311–316. [PubMed: 9699885]

Naray-Fejes-Toth A, Fejes-Toth G. Novel mouse strain with Cre recombinase in 11beta-hydroxysteroid dehydrogenase-2-expressing cells. Am J Physiol Renal Physiol. 2007; 292:F486–494. [PubMed: 16896181]

Pian P, Bucchi A, Robinson RB, Siegelbaum SA. Regulation of gating and rundown of HCN hyperpolarization-activated channels by exogenous and endogenous PIP2. J Gen Physiol. 2006; 128:593–604. [PubMed: 17074978]

Picelli S, Faridani OR, Bjorklund AK, Winberg G, Sagasser S, Sandberg R. Full-length RNA-seq from single cells using Smart-seq2. Nat Protoc. 2014; 9:171–181. [PubMed: 24385147]

Qu Y, Rogers J, Tanada T, Scheuer T, Catterall WA. Molecular determinants of drug access to the receptor site for antiarrhythmic drugs in the cardiac Na+ channel. Proc Natl Acad Sci U S A. 1995; 92:11839–11843. [PubMed: 8524860]

Ren D. Sodium leak channels in neuronal excitability and rhythmic behaviors. Neuron. 2011; 72:899–911. [PubMed: 22196327]

Rowland NE, Fregly MJ. Characteristics of thirst and sodium appetite in mice (Mus musculus). Behav Neurosci. 1988; 102:969–974. [PubMed: 3063282]

Sakai RR, Nicolaidis S, Epstein AN. Salt appetite is suppressed by interference with angiotensin II and aldosterone. Am J Physiol. 1986; 251:R762–768. [PubMed: 3532826]

Shin JW, Geerling JC, Loewy AD. Vagal innervation of the aldosterone-sensitive HSD2 neurons in the NTS. Brain Res. 2009; 1249:135–147. [PubMed: 19010311]

Southan C, Sharman JL, Benson HE, Faccenda E, Pawson AJ, Alexander SP, Buneman OP, Davenport AP, McGrath JC, Peters JA, et al. The IUPHAR/BPS Guide to PHARMACOLOGY in 2016: towards curated quantitative interactions between 1300 protein targets and 6000 ligands. Nucleic Acids Res. 2016; 44:D1054–1068. [PubMed: 26464438]

Tong Q, Ye CP, Jones JE, Elmquist JK, Lowell BB. Synaptic release of GABA by AgRP neurons is required for normal regulation of energy balance. Nat Neurosci. 2008; 11:998–1000. [PubMed: 19160495]

Usoskin D, Furlan A, Islam S, Abdo H, Lonnerberg P, Lou D, Hjerling-Leffler J, Haeggstrom J, Kharchenko O, Kharchenko PV, et al. Unbiased classification of sensory neuron types by large-scale single-cell RNA sequencing. Nat Neurosci. 2015; 18:145–153. [PubMed: 25420068]

Viengchareun S, Le Menuet D, Martinerie L, Munier M, Pascual-Le Tallec L, Lombes M. The mineralocorticoid receptor: insights into its molecular and (patho)physiological biology. Nucl Recept Signal. 2007; 5:e012. [PubMed: 18174920]

Vong L, Ye C, Yang Z, Choi B, Chua S Jr, Lowell BB. Leptin action on GABAergic neurons prevents obesity and reduces inhibitory tone to POMC neurons. Neuron. 2011; 71:142–154. [PubMed: 21745644]

Wahl-Schott C, Biel M. HCN channels: structure, cellular regulation and physiological function. Cell Mol Life Sci. 2009; 66:470–494. [PubMed: 18953682]

Yang CF, Chiang MC, Gray DC, Prabhakaran M, Alvarado M, Juntti SA, Unger EK, Wells JA, Shah NM. Sexually dimorphic neurons in the ventromedial hypothalamus govern mating in both sexes and aggression in males. Cell. 2013; 153:896–909. [PubMed: 23663785]

Zimmerman CA, Lin YC, Leib DE, Guo L, Huey EL, Daly GE, Chen Y, Knight ZA. Thirst neurons anticipate the homeostatic consequences of eating and drinking. Nature. 2016; 537:680–684. [PubMed: 27487211]

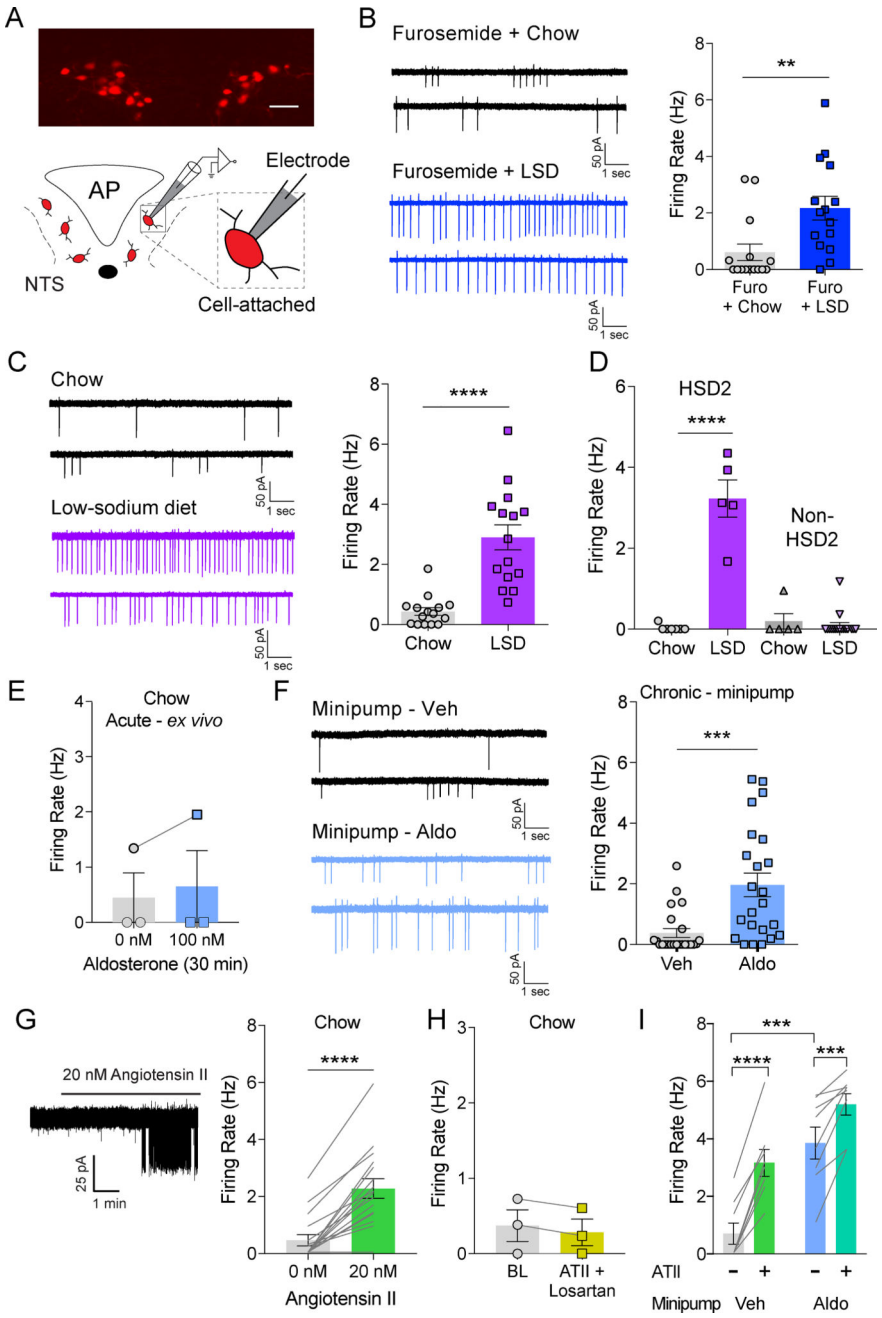

Figure 1. NTS^{HSD2} neuron activation by sodium deficiency and hormones

See also Table S1 & Figures S1–S2. All recordings were performed in the presence of synaptic blockers. Data are presented as mean ± SEM.

A) NTS *Hsd11b2-Cre*::Ai9tdTomato expression (top) and schematic of cell-attached recordings (bottom; AP = area postrema).

B) Representative cell-attached recordings of NTS^{HSD2} neurons from mice treated with furosemide and fed standard chow (Chow; top left) or low-sodium diet (LSD; bottom left), and summary of action potential (AP) firing rates (right; n = 15 neurons from 3 mice/condition). Unpaired two-tailed t-test, $^{**}P < 0.01$.

C) Representative cell-attached recordings of NTS^{HSD2} neurons from mice fed Chow (top left) or LSD (bottom left) for 8–12 days, and summary of AP firing rates (right; n = 15 neurons from 3 mice/condition). Unpaired two-tailed t-test, $^{****}P < 0.0001$.
D) AP firing rates of NTS^{HSD2} (HSD2) and neighboring NTS (non-HSD2) neurons from animals fed Chow or LSD (Chow: n = 7 HSD2 neurons and n = 5 non-HSD2 neurons from 2 mice; LSD: n = 5 HSD2 neurons and n = 17 non-HSD2 neurons from 2 mice). One-way ANOVA with posthoc analysis by Tukey's multiple comparisons test, $^{****}P < 0.0001$.
E) AP firing rates of NTS^{HSD2} neurons from Chow-fed mice before and after bath application of aldosterone for 30 minutes (n = 3 neurons from 2 mice).
F) Representative cell-attached recordings of NTS^{HSD2} neurons from animals with chronic vehicle (top left) or aldosterone (bottom left) minipump infusion for 8–12 days, and summary of AP firing rates (right; n = 23 neurons from 5 mice/condition). Unpaired two-tailed t-test, $^{*}P < 0.05$.
G) Representative cell-attached recording (left) and summary of AP firing rates of NTS^{HSD2} neurons from Chow-fed mice before and after bath application of angiotensin II (right; ATII; n = 16 neurons from 5 mice). Paired two-tailed t-test, $^{**}P < 0.01$.
H) AP firing rates of NTS^{HSD2} neurons from Chow-fed mice before and after application of ATII in presence of losartan (n = 3 neurons from 2 mice).
I) AP firing rates of NTS^{HSD2} neurons from Chow-fed mice implanted with osmotic pumps before and after application of ATII (n = 8 neurons from 2 mice/condition). Two-way repeated measures ANOVA with posthoc analysis by Sidak's multiple comparisons test $^{***}P < 0.001$, $^{****}P < 0.0001$.

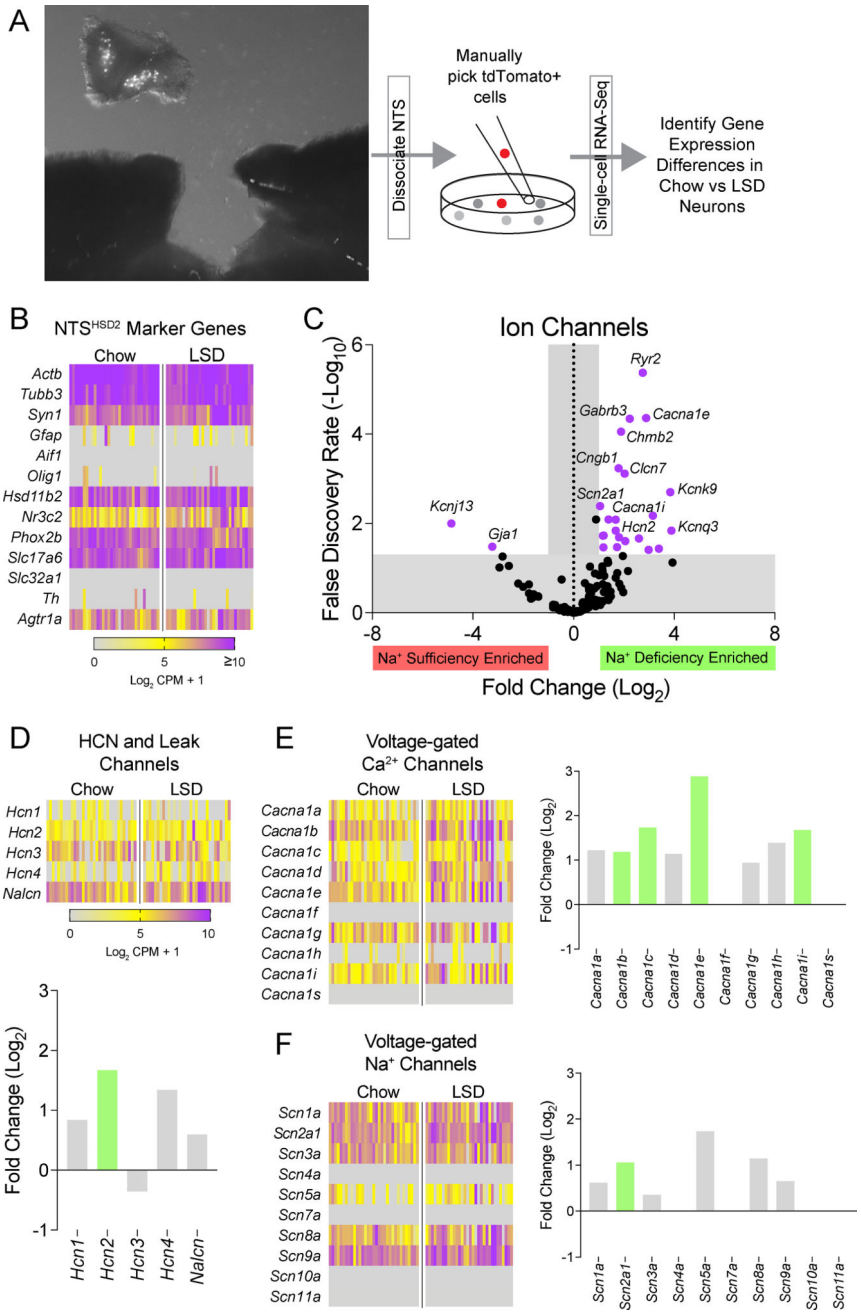

Figure 2. RNA sequencing of NTS^{HSD2} neurons

See also Tables S2–S3 & Figures S3–S4.

A) NTS tissue dissection and schematic of the methodological approach for single neuron RNA sequencing of NTS^{HSD2} neurons from *Hsd11b2-Cre*::Ai9tdTomato mice.

B) Heatmap showing single neuron expression patterns for neuronal, glial, NTS, and NTS^{HSD2} neuron-specific marker genes from standard chow (Chow) and low-sodium diet (LSD)-fed mice.

C) Volcano plot of IUPHAR ion channel genes affected by Na^+ deprivation. Dots outside the grey shaded region colored purple represent ion channel genes with significantly altered

expression in response to Na^+ deprivation (Log_2 Fold Change > 1 or < −1, and False Discovery Rate < 0.05).

D) Heatmap showing single neuron expression patterns for hyperpolarization-activated cyclic nucleotide-gated (*Hcn*) channels and the cation leak channel, *Nalcn*, in NTS^{HSD2} neurons from Chow- and LSD-fed mice (top), and Log_2 Fold Change values for each channel gene (bottom). Na^+ deficiency-enriched genes are depicted with green bars. No genes were suppressed by Na^+ deficiency.

E) Heatmap showing single neuron expression patterns for voltage-gated Ca^{2+} channels in NTS^{HSD2} neurons from Chow- and LSD-fed mice (left) and Log_2 Fold Change values for each channel (right). Na^+ deficiency-enriched genes are depicted with green bars. No genes were suppressed by Na^+ deficiency.

F) Heatmap showing single neuron expression patterns for voltage-gated Na^+ channels in NTS^{HSD2} neurons from Chow- and LSD-fed mice (left) and Log_2 Fold Change values for each channel (right). Na^+ deficiency-enriched genes are depicted with green bars. No genes were suppressed by Na^+ deficiency.

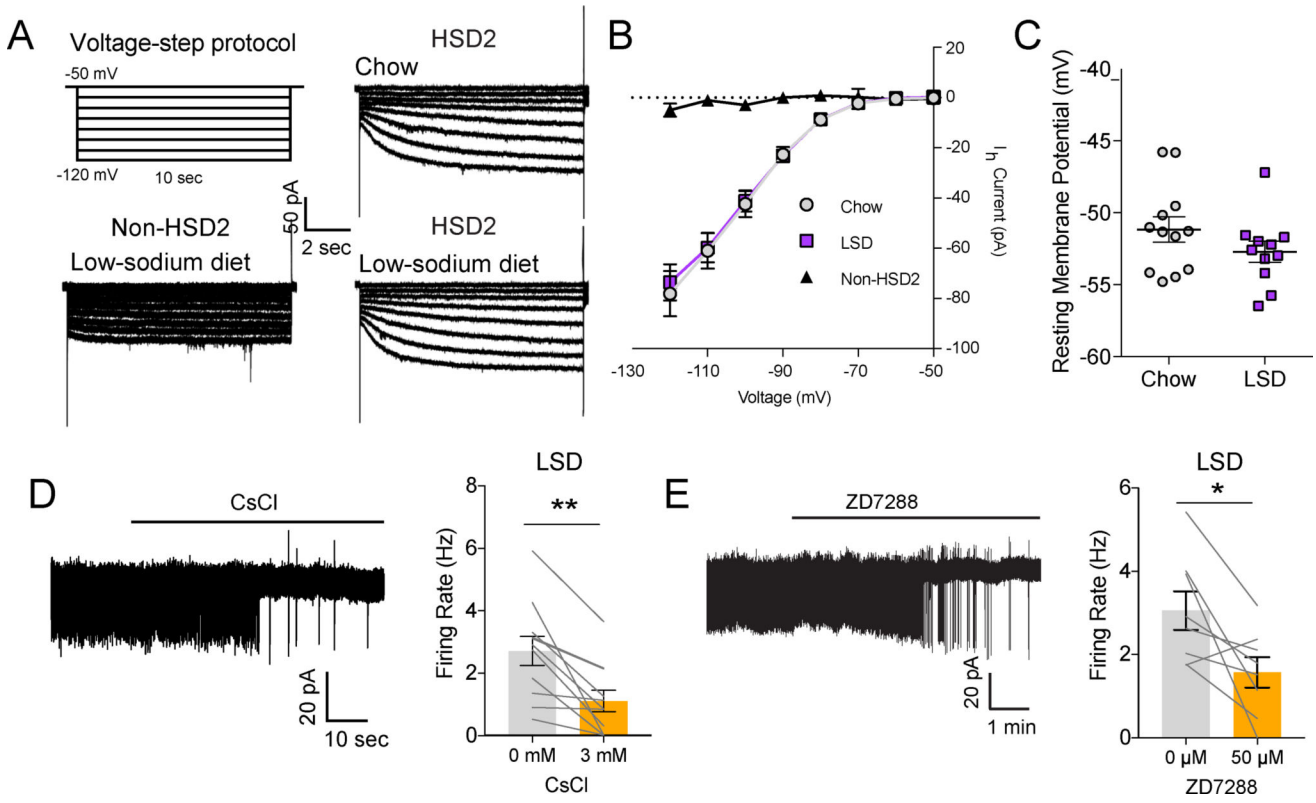

Figure 3. HCN channels are permissive for NTS^{HSD2} neuron pacemaker activity

All recordings were performed in the presence of synaptic blockers. Data are presented as mean ± SEM.

A) Hyperpolarizing voltage-step protocol for measuring I_h (top left), and representative I_h recordings in NTS^{HSD2} (HSD2; right) and neighboring NTS (non-HSD2; bottom left) neurons from mice fed standard chow (Chow) or low-sodium diet (LSD).

B) Summary of I_h in NTS HSD2 and non-HSD2 neurons from Chow- and LSD-fed mice (Non-HSD2: n = 8 neurons from 2 mice; Chow: n = 15 HSD2 neurons from 4 mice; LSD: n = 15 HSD2 neurons from 4 mice).

C) Resting membrane potential of NTS^{HSD2} neurons from Chow- and LSD-fed mice (Chow: n = 12 neurons from 2 mice; LSD: n = 11 neurons from 2 mice).

D) Representative cell-attached recording (left) and summary (right) of action potential (AP) firing rates of NTS^{HSD2} neurons from Na^+-deprived mice before and after CsCl application (n = 11 neurons from 3 mice). Paired two-tailed t-test, $^{**}P < 0.01$.

E) Representative cell-attached recording (left) and summary (right) of AP firing rates of NTS^{HSD2} neurons from Na^+-deprived mice before and after ZD7288 application (n = 8 neurons from 4 mice). Paired two-tailed t-test, $^{*}P < 0.05$.

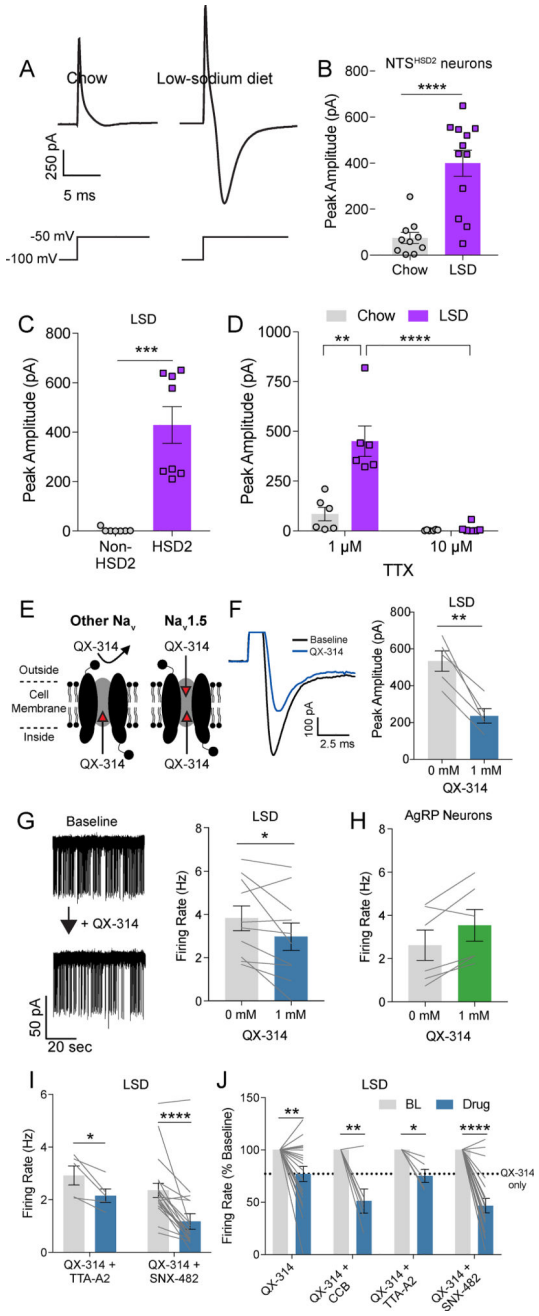

Figure 4. TTX-resistant sodium current promotes state-dependent NTS^{HSD2} neuron pacemaker activity

See also Figure S5. All recordings were performed in the presence of synaptic blockers. Data are presented as mean ± SEM.

A) Representative evoked currents recorded in 1 µM TTX of NTS^{HSD2} neurons (top) from mice fed standard chow (Chow) or low-sodium diet (LSD) with illustration of voltage-step protocol (bottom).

B) Summary of NTS^{HSD2} neuron peak evoked current amplitudes recorded in 1 µM TTX from Chow- and LSD-fed mice (Chow: n = 10 neurons from 3 mice; LSD: n = 12 neurons from 3 mice). Unpaired two-tailed t-test, ****$P < 0.0001$.

C) Peak evoked current amplitudes recorded in 1 μM TTX of NTS^{HSD2} (HSD2) and neighboring NTS (non-HSD2) neurons from Na^+-deprived mice (n = 7 HSD2 neurons and 8 non-HSD2 neurons from 3 mice). Unpaired two-tailed t-test, $^{***}P < 0.001$.

D) NTS^{HSD2} neuron peak evoked current amplitude from Chow- and LSD-fed mice with 1 μM or 10 μM TTX in the bath (n = 6 neurons from 3 mice/condition). Two-way repeated measures ANOVA with posthoc analysis by Sidak's multiple comparisons test, $^{**}P < 0.01$, $^{****}P < 0.0001$.

E) Schematic depicting the pharmacological action of QX-314 on voltage-gated Na^+ channels.

F) Example trace (left) and summary (right) of peak evoked current amplitude before and after QX-314 treatment in NTS^{HSD2} neurons from Na^+-deprived mice (n = 5 neurons from 2 mice). Paired two-tailed t-test, $^{**}P < 0.01$.

G) Representative cell-attached recording (left) and summary (right) of action potential (AP) firing rates of NTS^{HSD2} neurons from Na^+-deprived mice pre- and post-QX-314 application (n = 10 neurons from 4 mice). Paired two-tailed t-test, $^{*}P < 0.05$.

H) AP firing rates of hypothalamic AgRP neurons from fasted mice pre- and post-QX-314 application (n = 6 neurons from 2 mice).

I) AP firing rates of NTS^{HSD2} neurons from Na^+-deprived mice pre- and post-application of QX-314 and TTA-A2 (n = 5 neurons from 3 mice) or QX-314 and SNX-482 (n = 19 neurons from 8 mice). Paired two-tailed t-test, $^{*}P < 0.05$, $^{****}P < 0.0001$.

J) AP firing rates of NTS^{HSD2} neurons from Na^+-deprived mice normalized to baseline (BL; % baseline) pre- and post-drug application of QX-314 (n = 19 neurons from 8 mice), QX-314 and a Ca^{2+} channel blocker cocktail (CCB; n = 6 neurons from 3 mice), QX-314 and TTA-A2 (n = 5 neurons from 3 mice), or QX-314 and SNX-482 (n = 19 neurons from 8 mice). Paired two-tailed t-test, $^{*}P < 0.05$, $^{**}P < 0.01$, $^{****}P < 0.0001$.

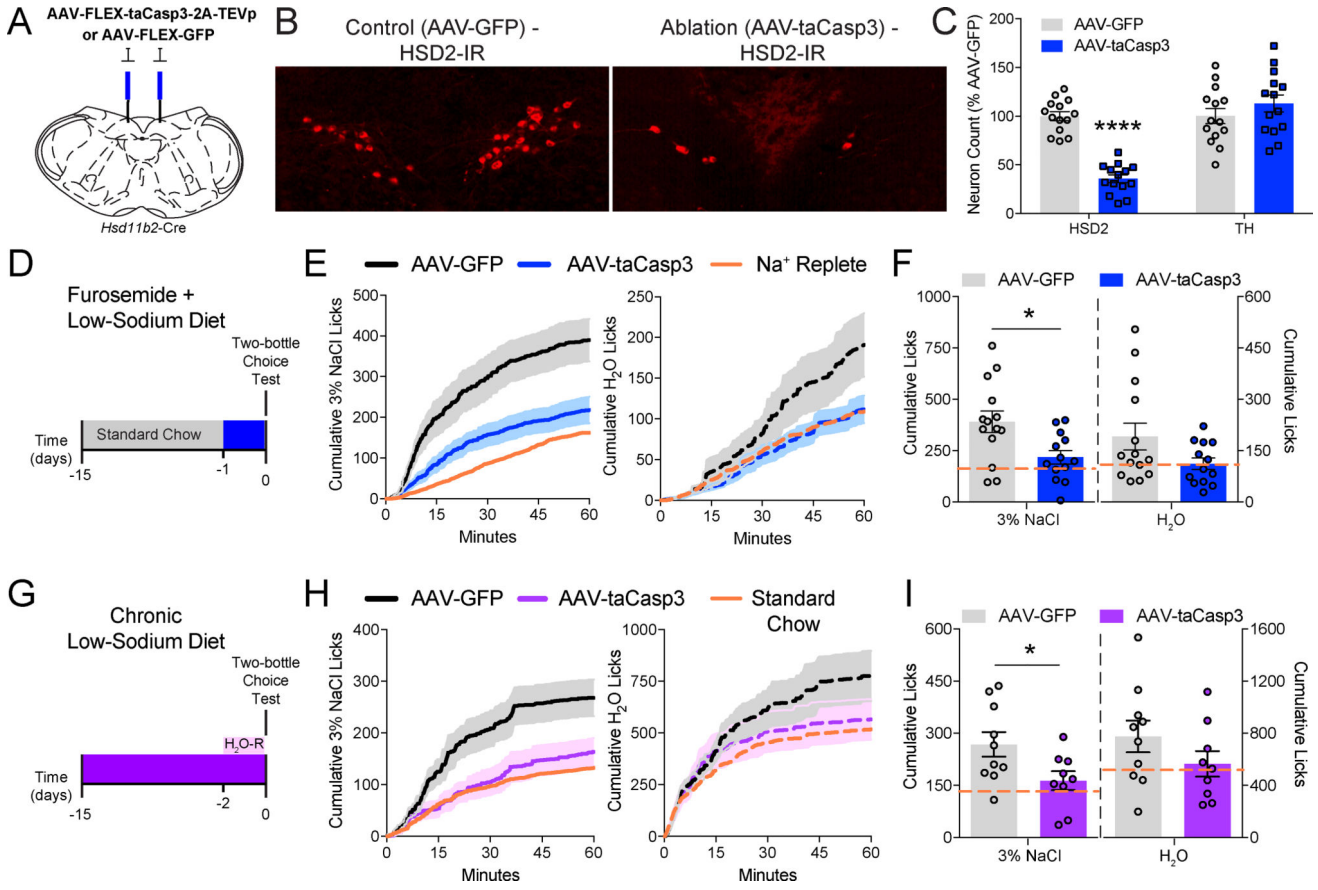

Figure 5. Specific ablation of NTS^{HSD2} neurons impairs sodium appetite

Data are presented as mean ± SEM.

A) Schematic of AAV-FLEX-taCasp3-2A-TEVp or AAV-FLEX-GFP injections.

B) Representative HSD2 immunoreactivity (HSD2-IR) in the NTS of AAV-FLEX-GFP (AAV-GFP; left) and AAV-FLEX-taCasp3-2A-TEVp (AAV-taCasp3; right) injected mice.

C) Summary of AAV-taCasp3 ablation efficiency and specificity by counts of NTS HSD2 and tyrosine hydroxylase (TH) positive neurons (n = 13–14 mice/group). Unpaired two-tailed t-test, ****$P < 0.0001$.

D) Schematic of the experimental protocol used for furosemide-induced Na^+ depletion.

E) Time course of 3% NaCl licking (left) or H_2O licking (right) following Na^+ depletion in AAV-GFP and AAV-taCasp3 injected animals. Orange line depicts the mean intake of Na^+-replete animals injected with furosemide and fed standard chow.

F) Summary of 60-minute Na^+ appetite test following Na^+ depletion in AAV-GFP and AAV-taCasp3 injected animals (n = 13–14 mice/group). Orange line depicts the mean intake of Na^+-replete animals injected with furosemide and fed standard chow. Unpaired two-tailed t-test, *$P < 0.05$.

G) Schematic of the experimental protocol used for chronic dietary Na^+ deprivation (H_2O-R = H_2O-restriction).

H) Time-course of 3% NaCl licking (left) or H_2O licking (right) following dietary Na^+ deprivation in H_2O-restricted animals injected with AAV-GFP or AAV-taCasp3. Orange line depicts the mean intake of Na^+-replete animals fed standard chow.

I) Summary of 60-minute Na^+ appetite test following dietary Na^+ deprivation in H_2O-restricted animals injected with AAV-GFP or AAV-taCasp3 (n = 9–10 mice/group). Orange line depicts the mean intake of Na^+-replete animals fed standard chow. Unpaired two-tailed t-test, $*P < 0.05$. Unpaired two-tailed t-test, $*P < 0.05$.

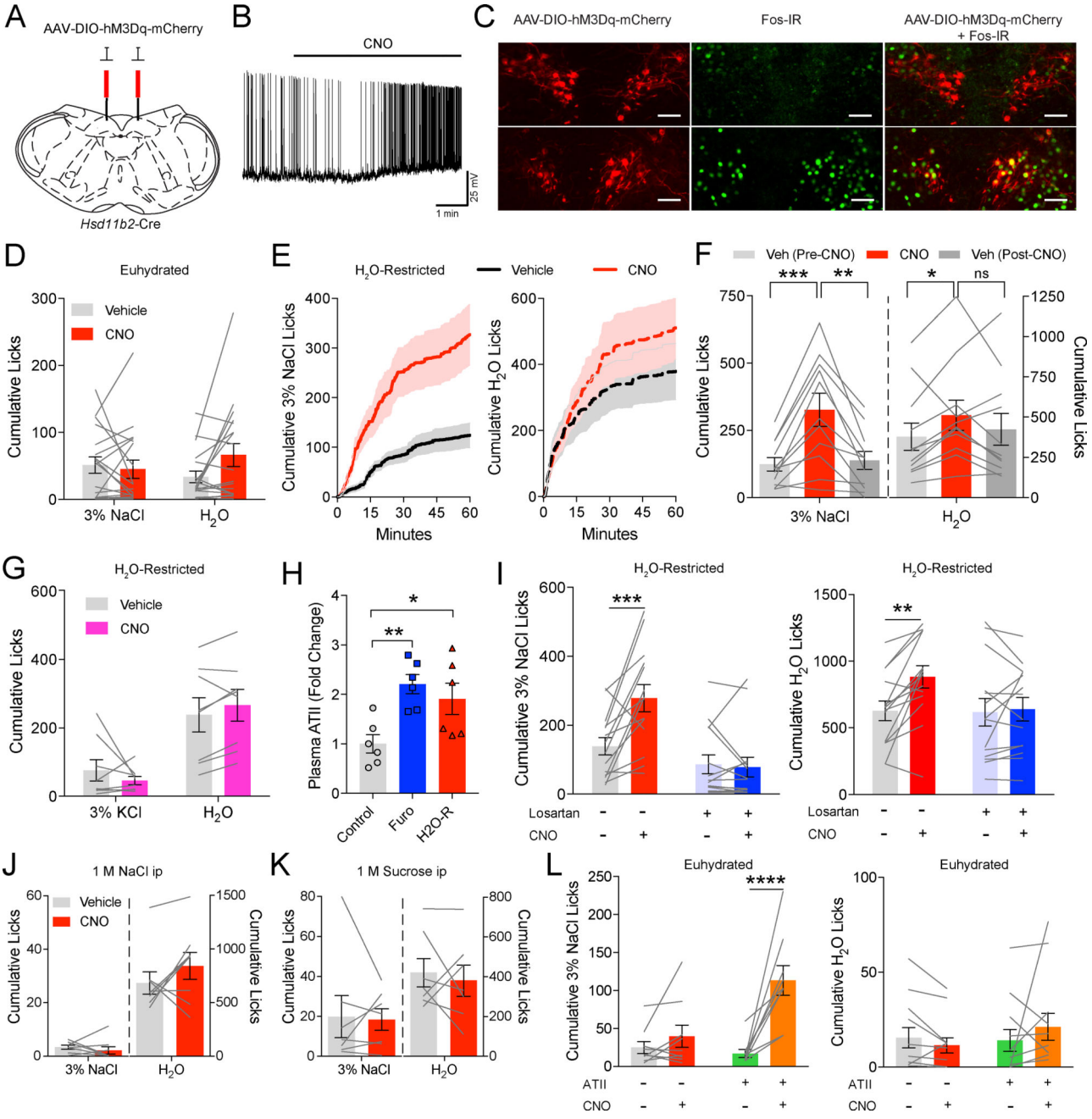

Figure 6. NTS^{HSD2} neuron stimulation synergizes with angiotensin II signaling to drive sodium appetite

See also Figure S6. Data are presented as mean ± SEM.

A) Schematic of AAV-DIO-hM3Dq-mCherry injections.

B) Representative recording of an hM3Dq-expressing NTS^{HSD2} neuron pre- and post-CNO (5 μM) application.

C) NTS hM3Dq-mCherry expression in *Hsd11b2-Cre* mice (left), Fos immunoreactivity (Fos-IR; middle), and hM3Dq-mCherry + Fos-IR (right) in vehicle (top) or CNO (bottom) treated mice.

D) 3% NaCl and H_2O licking behavior over 60 minutes after CNO/hM3Dq stimulation of NTS^{HSD2} neurons in euhydrated mice (n = 18 mice).

E) Time course of 3% NaCl licking (left) or H_2O licking (right) following CNO/hM3Dq stimulation of NTS^{HSD2} neurons in H_2O-restricted mice.

F) Summary of 60 minutes of licking behavior following CNO/hM3Dq stimulation of NTS^{HSD2} neurons in H_2O-restricted mice (n = 11 mice). Two-way repeated measures ANOVA followed by Tukey's multiple comparisons test, $*P < 0.05$, $**P < 0.01$, $***P < 0.001$.

G) 3% KCl and H_2O licking behavior over 60 minutes following chemogenetic activation of NTS^{HSD2} neurons in H_2O-restricted mice (n = 8 mice).

H) Plasma ATII levels (fold change) under control, furosemide + LSD (Furo), and H_2O-restricted (H_2O-R) conditions (n = 6 mice/group). One-way ANOVA with posthoc analysis by Dunnett's multiple comparisons test, $*P < 0.05$, $**P < 0.01$.

I) 3% NaCl (left) and H_2O (right) licking behavior over 60 minutes following CNO/hM3Dq stimulation of NTS^{HSD2} neurons in H_2O-restricted animals ± the AT1aR antagonist losartan (20 mg/kg; n = 14 mice). Two-way repeated measures ANOVA followed by Tukey's multiple comparisons test, $**P < 0.01$, $***P < 0.001$.

J) 3% NaCl and H_2O licking behavior over 60 minutes after CNO/hM3Dq stimulation of NTS^{HSD2} neurons and injection of 1 M NaCl (n = 8 mice).

K) 3% NaCl and H_2O licking behavior over 60 minutes after CNO/hM3Dq stimulation of NTS^{HSD2} neurons and injection of 1 M sucrose (n = 7 mice).

L) 3% NaCl (left) and H_2O (right) licking behavior over 60 minutes following CNO/hM3Dq stimulation of NTS^{HSD2} neurons under euhydrated conditions ± ATII injections (0.25 mg/kg; n = 8 mice). Two-way repeated measures ANOVA followed by Tukey's multiple comparisons test, $****P < 0.0001$.

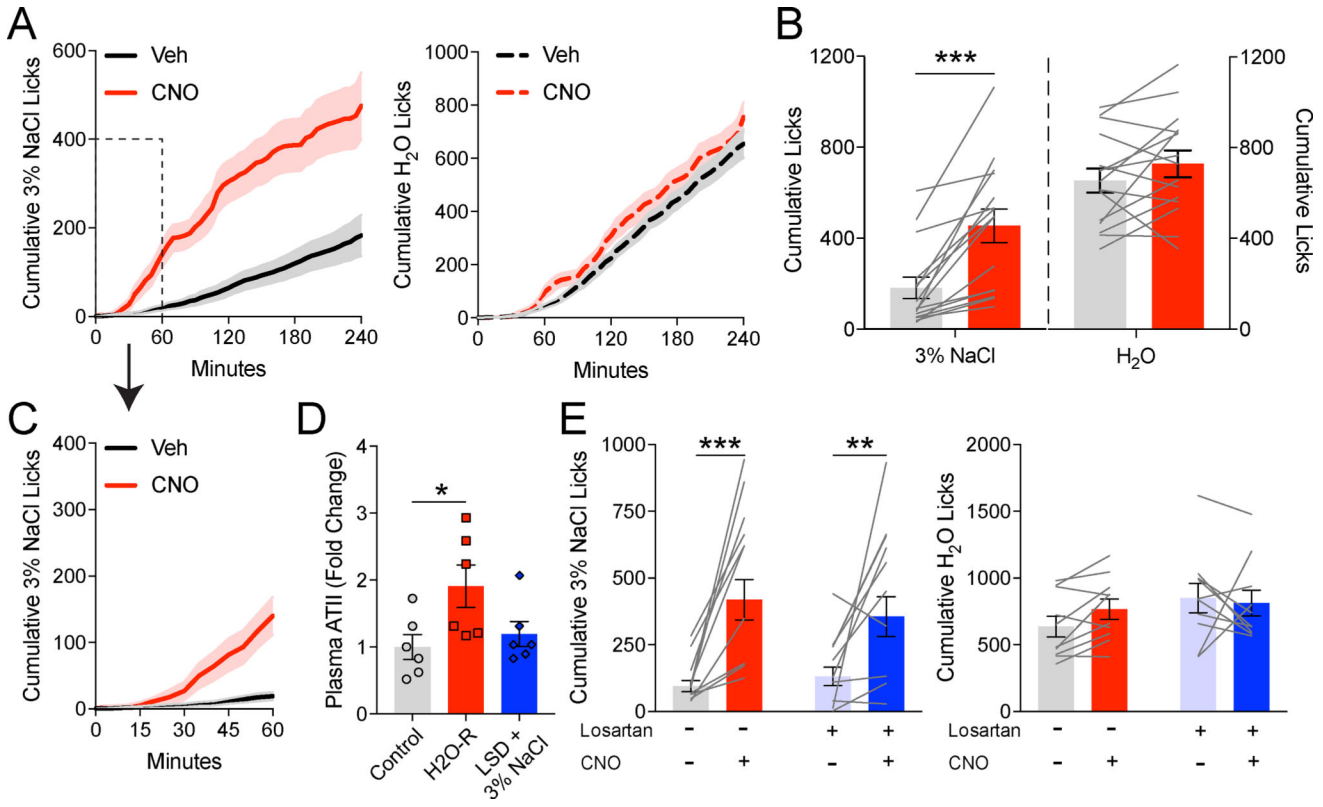

Figure 7. NTS^{HSD2} neuron stimulation can promote sodium ingestion without water restriction

Data are presented as mean ± SEM.

A) Time course of 3% NaCl (left) or H_2O (right) licking behavior following CNO/hM3Dq stimulation of NTS^{HSD2} neurons in experiments following the protocol described by Jarvie and Palmiter (2017).

B) Summary of licking behavior over 4 hours following CNO/hM3Dq stimulation of NTS^{HSD2} neurons in experiments following the protocol described by Jarvie and Palmiter (n = 15 mice). Paired two-tailed t-test, ***P < 0.001.

C) Time course of 3% NaCl licking behavior within first hour (inset in A).

D) Plasma ATII levels (fold change) under control, H_2O-restricted (H_2O-R), and LSD + 3% NaCl (Jarvie and Palmiter, 2017) conditions (n = 6 mice/group). Control and H_2O-R data are also depicted in Figure 6H. One-way ANOVA with posthoc analysis by Dunnett's multiple comparisons test, *$P < 0.05$, **$P < 0.01$.

E) 3% NaCl (left) and H_2O (right) licking behavior over 4 hours following CNO/hM3Dq stimulation of NTS^{HSD2} neurons ± the AT1aR antagonist losartan (20 mg/kg) in experiments following the protocol described by Jarvie and Palmiter (n = 6 mice). Two-way repeated measures ANOVA followed by Tukey's multiple comparisons test, **$P < 0.01$, ***$P < 0.001$.

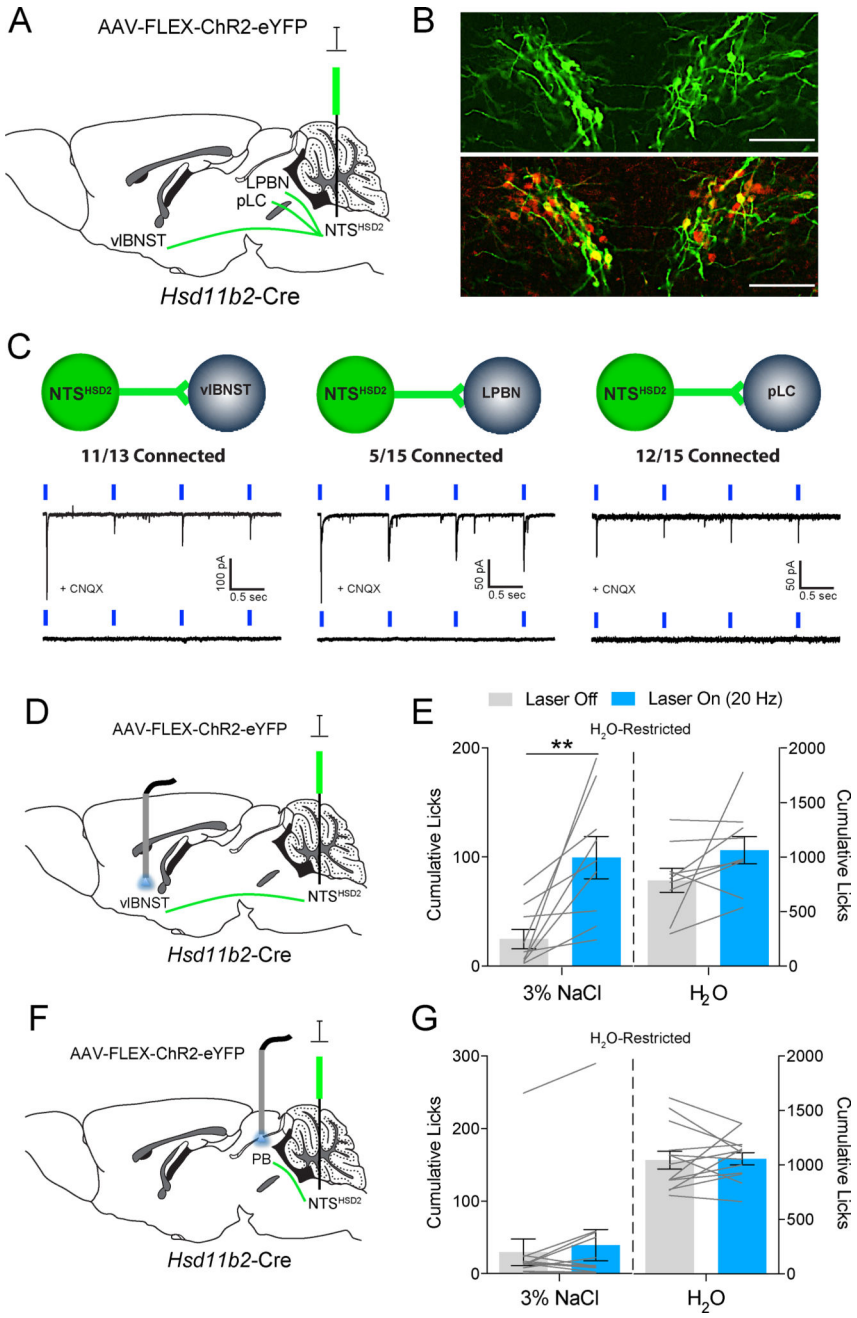

Figure 8. Stimulation of NTS^{HSD2} neuron projections to the vlBNST produce sodium appetite in H_2O-restricted mice

See also Figure S7. Data are presented as mean ± SEM.

A) Schematic of AAV-FLEX-ChR2-eYFP injections.

B) Validation of ChR2-eYFP expression in NTS^{HSD2} neurons from *Hsd11b2-Cre* mice (top) with HSD2 immunoreactivity (HSD2-IR; bottom).

C) Schematics and representative traces from ChR2-assisted circuit mapping experiments of NTS^{HSD2} → vlBNST (n = 13 neurons from 2 mice; left), NTS^{HSD2} → LPBN (n = 15

neurons from 2 mice; middle), and $NTS^{HSD2} \rightarrow$ pLC (n = 15 neurons from 2 mice; right). Light-evoked EPSCs were blocked by CNQX (bottom traces).

D) Schematic of optogenetic NTS^{HSD2} neuron terminal stimulation in the vlBNST.

E) 3% NaCl (left) and H_2O (right) licking behavior over 20 minutes of optogenetic stimulation of NTS^{HSD2} neuron projections to the vlBNST in H_2O-restricted mice (n = 9 mice). Paired two-tailed t-test, $^{**}P < 0.01$.

F) Schematic of optogenetic NTS^{HSD2} neuron terminal stimulation in the parabrachial complex (PB).

G) 3% NaCl (left) or H_2O (right) licking behavior over 20 minutes of optogenetic stimulation of NTS^{HSD2} neuron projections to the PB in H_2O-restricted mice (n = 13 mice).